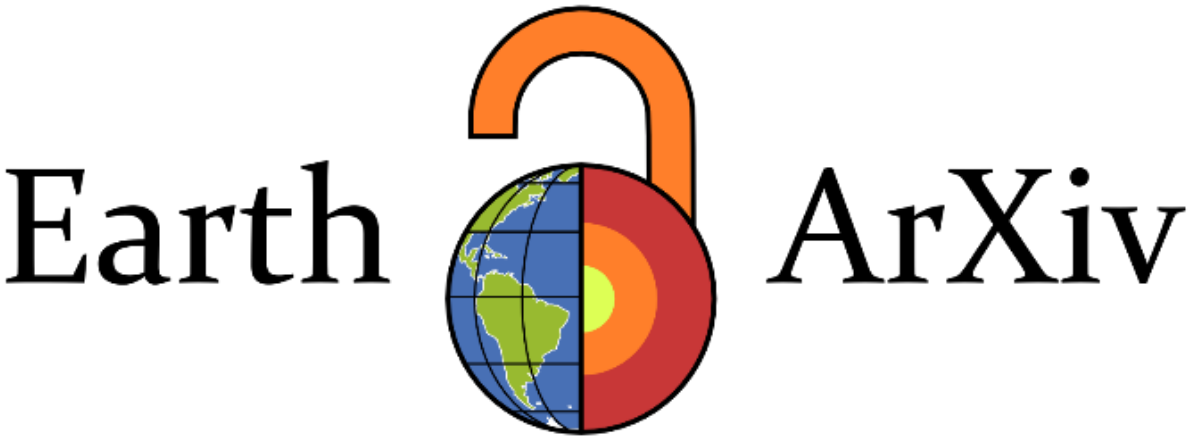

Evaluating the potential of SMART subsea cable pressure sensors to constrain Subpolar North Atlantic circulation variability through Observing System Simulation Experiments

Matthew C. Goldberg,[a] An T. Nguyen,[a] Helen Pillar,[a] , Bruce M. Howe,[c] Patrick Heimbach,[a,b]

[a] *Oden Institute for Computational Engineering and Sciences, The University of Texas at Austin, 201 E. 24th Street, C0200, Austin, TX 78712, United States of America*

[b] *Jackson School of Geosciences, University of Texas at Austin* [c] *University of Hawai'i at Manoa - JTF SMART Cables, 2525 Correa Rd. HIG 109B, Honolulu, HI 96822, United States of America*

Corresponding author: Matthew C. Goldberg, matthew.goldberg10@utexas.edu

ABSTRACT: Bolstering global ocean observing infrastructure is critical for understanding, quantifying, and predicting Earth's climate variability and change. The emerging SMART (Science Monitoring And Reliable Telecommunications) Subsea Cables present an opportunity to acquire high-frequency, seafloor-based observations of ocean variables, encouraging assessment of their value prior to deployment. We conduct Observing System Simulation Experiments (OSSEs) to quantify potential for constraining ocean circulation using simulated SMART sensor data from a proposed cable in the Subpolar North Atlantic. Synthetic daily SMART ocean bottom pressure anomaly observations from a high-resolution global "nature run" are assimilated into a regional ocean model. Model-data misfit is reduced via gradient-based adjustments to atmospheric control variables. Synthetic data value is then quantified via the error reduction and improved skill between the regional model and the nature run. Assimilation of synthetic SMART data improves regional estimates of ocean bottom pressure as well as unobserved quantities such as barotropic (depth-integrated) transport and Arctic freshwater exports, demonstrating the SMART system's potential to constrain basin-scale ocean circulation. On annual time scales SMART cables are shown to complement satellite altimetry data by providing unique constraints on sub-monthly and coastal oceanic mass transport, leading to larger localized reductions in ocean bottom pressure uncertainty. Atmospheric pressure, followed by zonal and meridional surface winds, are identified as the primary control variables driving daily bottom pressure anomaly correction, which is understood through the inverse barometer effect. Our results underscore the value of high-frequency seafloor pressure data for improving estimates of climate-relevant ocean transports and highlight their promise for enhancing the spatiotemporal resolution of ocean mass distribution and circulation estimates.

Significance Statement

The ocean plays a central role in regulating Earth's climate, but many important processes are poorly measured because existing observing systems do not adequately sample the global ocean. This study explores how commercial seafloor telecommunication cables equipped with scientific sensors could help fill those gaps. Using computer simulations, we show that daily seafloor pressure measurements can reduce uncertainty in ocean mass redistribution and freshwater transport throughout the Subpolar North Atlantic, a region critical for climate. Our results suggest that sensor-equipped cables provide a complementary constraint to existing satellite-based ocean bottom pressure measurements on the daily to monthly timescales considered. We also find that changes in surface atmospheric pressure and winds strongly influence these signals. These findings encourage further investigation of the potential value of SMART for sustainable long-term climate monitoring and prediction.

1. Introduction

The Science Monitoring And Reliable Telecommunications (SMART) subsea cable initiative represents a new frontier in ocean observation, enabling high-frequency seafloor monitoring through telecommunication infrastructure (Howe et al. 2019). As part of the United Nations Decade of Ocean Science for Sustainable Development, the Joint Task Force on SMART cable systems was established in 2012 by the International Telecommunication Union (ITU), the World Meteorological Organization (WMO), and the Intergovernmental Oceanographic Commission of UNESCO (UNESCO-IOC). It is supported by more than 400 volunteer stakeholders and works to enhance the Global Ocean Observing System (GOOS) by integrating scientific sensors into newly deployed subsea fiber optic cables. As one of four emerging GOOS networks complementing thirteen established ones, SMART cables will host instruments such as thermometers, seismic accelerometers, and pressure sensors, spaced approximately 70 to 150 km apart, with exact spacing dictated by commercial deployment constraints. These sensor packages cannot be attached or augmented once the cable is in place, a design limitation driven by stringent regulations from the telecommunications industry. This encourages rigorous assessment of SMART's potential value in advance of cable deployment to best leverage opportunity for enhancing ocean observing. Here, we conduct observing system simulation experiments (OSSEs) to quantify how in situ ocean bottom pressure

(OBP) measurements from SMART cables can improve understanding of ocean circulation and better constrain the time-evolving ocean state.

OBP reflects the mass of the overlying water column and atmosphere. It varies in response to circulation change, tides, surface momentum and mass flux (precipitation, evaporation, runoff, and glacial melt). Currently, large-scale OBP variations are primarily observed from space via the Gravity Recovery and Climate Experiment (GRACE) and its follow-on mission GRACE-FO, which infer monthly-mean OBP anomalies p_b from changes in Earth's gravity field (Tapley et al. 2004, 2019; Landerer et al. 2020). GRACE-based monthly p_b products have supported extensive investigation of seasonal to interannual variability in sea level, ocean heat content, and ocean circulation (see review by Tapley et al. 2019). These products, however, show both non-negligible discrepancies arising from processing differences (Blazquez et al. 2018) and significant errors resulting from high frequency signal aliasing (Quinn and Ponte 2011). GRACE's effective spatial resolution of roughly 300 km also limits application for coastal and mesoscale oceanography. Our focus on OBP is motivated by the potential for SMART to complement GRACE by providing high-frequency in situ p_b estimates, including in regions poorly resolved by GRACE (e.g., coasts, straits, marginal seas).

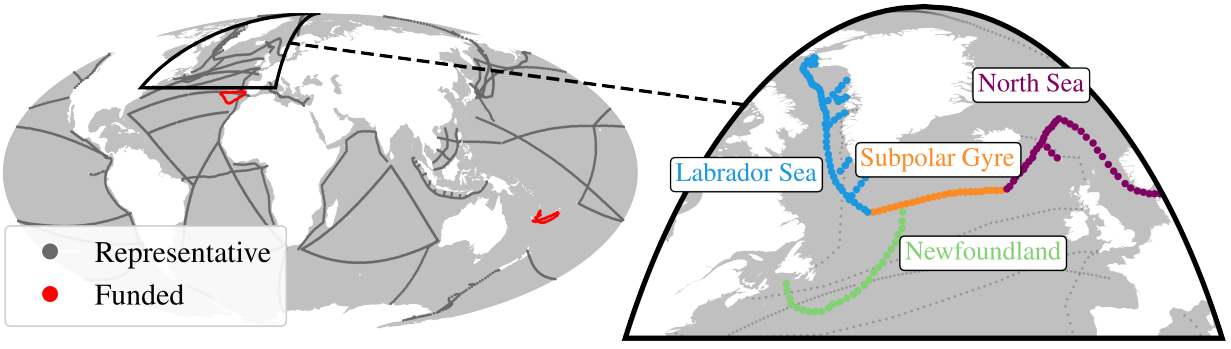

FIG. 1. (Left) Representative future global SMART cable network (gray) and funded systems in development (red). (Right) Subpolar North Atlantic cable and partial cables used in this study.

Our work builds on previous investigations of the value of OBP observations within data assimilation (DA) frameworks by Köhl et al. (2012), Saynisch et al. (2015), and Ponte et al. (2026). Köhl et al. (2012) assessed the impact of assimilating monthly GRACE data into a 1-degree global ocean state estimate and found that adjustments to the model's basin-scale OBP correlate with changes in

the model's barotropic transport, except near the equator where geostrophy breaks down, and along the coasts where steric sea level changes are large (Landerer et al. 2007) and GRACE's coarse resolution becomes a limiting factor. Improvements were shown to be largest in the subtropical gyres and polar latitudes, but were sensitive to the OBP product used, with products differing regionally and close to land. Saynisch et al. (2015) used an ensemble Kalman Filter to demonstrate improved model daily OBP when assimilating GRACE data. The improvement was associated with wind-driven adjustments to the barotropic circulation. Improvements were particularly notable at high latitudes, consistent with Köhl et al. (2012). Ponte et al. (2026) expanded on these studies by interrogating the impacts of assimilating an extended OBP record from GRACE and GRACE-FO into a global state estimate, which additionally uses these data to constrain global mean ocean mass. They found improvements to both local and basin-scale OBP variability, factoring in the influence of non-oceanographic geophysical processes captured in GRACE data. These results demonstrate the benefit of GRACE for constraining large-scale mass redistribution while underscoring the limitations imposed by temporal resolution, observational gaps, and processing uncertainties.

Here, we seek to quantify the potential benefit of in situ OBP monitoring along SMART cables by conducting OSSEs within the Estimating the Climate and Circulation of the Ocean (ECCO) state estimation framework (Wunsch and Heimbach 2007; Forget et al. 2015; Fukumori et al. 2017). ECCO provides estimates of the time evolving ocean state via nonlinear least-squares optimization in which the model-data misfit is reduced by making iterative gradient-based adjustments to a set of independent, uncertain control variables. We examine both direct impacts of assimilation on local OBP fields and the impacts on remote quantities of interest (QoIs). In contrast with previous studies, we examine how OBP assimilation drives adjustments in these control variables and how these adjustments subsequently impact the ocean state. We focus on proposed SMART observations in the Subpolar North Atlantic (SPNA, Figs. 1 & 2), a region that is critically important for the Atlantic Meridional Overturning Circulation (AMOC) and susceptible to major transitions associated with varying Arctic-Atlantic exchanges and freshwater pathways (e.g., Bacon et al. 2022; Weijer et al. 2022). Importantly, observational (Lozier et al. 2017) and modeling (Kostov et al. 2021) studies have established that significant variability in SPNA overturning and associated transports of heat and freshwater (Li et al. 2024) occur on intraseasonal time scales, motivating sustained continuous monitoring. The dynamic environment and topographic complexity of the SPNA make it an ideal

proving ground for assessing the capacity of regional ocean models to assimilate high-frequency OBP data and improve estimates of key climate indicators such as overturning strength and volume transport through high latitude gateways.

The remainder of the paper is arranged as follows. Section 2 describes the OSSE design. OSSE results are shown in Section 3. This includes a discussion of model-data misfit reduction of p_b and improvement in unobserved QoIs, namely barotropic velocity and Arctic freshwater export. Section 4 discusses the dynamical mechanisms underpinning the OSSE results, outlining key atmospheric control adjustments and the role of the inverted barometer effect. Section 5 provides a summary of the work and future outlook.

2. Methods

Below we describe our OSSE design, including the data assimilation methodology and the configuration of both the nature run (NR) and the forecast model (FM). In an OSSE, a high-resolution NR is considered to represent the "true" system's state, e.g. the observed ocean. It provides a dataset from which synthetic observations are sampled. These synthetic observations are then assimilated into the FM accounting for their uncertainty. The impact of the observing system is quantified by comparing diagnostics of the pre- and post- assimilation FM states against the corresponding NR field (Hoffman and Atlas 2015; Zeng et al. 2020).

a. Data assimilation framework

Our OSSEs are performed in the ECCO framework using configurations of the MIT general circulation model (MITgcm, Marshall et al. 1997; Adcroft et al. 2004). State estimation amounts to solving an inverse problem in which the uncertain model input or control variables $\mathbf{u}$, comprising hydrographic initial conditions, surface atmospheric boundary conditions and ocean mixing parameters, are adjusted within their uncertainty to minimize the model misfit to all assimilated observations. Here, we consider only the atmospheric boundary condition subset, $\mathbf{u}_{\mathrm{BC}}$, of the full control vector. Control adjustments are determined by running the adjoint model, obtained via algorithmic differentiation (Giering and Kaminski 1998), to compute the gradient of the costfunction

J to all control variables, where

$$J(\mathbf{u}_{\mathrm{BC}}) = \underbrace{\frac{1}{2}(\mathbf{y}-\hat{\mathbf{y}})^{\mathrm{T}}\boldsymbol{\Gamma}_{\mathrm{obs}}^{-1}(\mathbf{y}-\hat{\mathbf{y}})}_{J_{\mathrm{misfit}}(\mathbf{u}_{\mathrm{BC}})} + \underbrace{\frac{1}{2}(\mathbf{u}_{\mathrm{BC}}-\mathbf{u}_{\mathrm{BC}}^{0})^{\mathrm{T}}\boldsymbol{\Gamma}_{\mathrm{BC}}^{-1}(\mathbf{u}_{\mathrm{BC}}-\mathbf{u}_{\mathrm{BC}}^{0})}_{J_{\mathrm{BC}}(\mathbf{u}_{\mathrm{BC}})}. \tag{1}$$

The first term in Eqn. 1 computes the uncertainty-weighted misfit between N observational data (or synthetic observations as done here) $\mathbf{y} = [y_1, \ldots, y_N]^T \in \mathbb{R}^N$ and model equivalents obtained via the parameter-to-observable map $\hat{\mathbf{y}} = \mathbf{Obs}(\mathbf{x}(\mathbf{u}_{\mathrm{BC}})) = [\mathbf{Obs}_1(\mathbf{x}(\mathbf{u}_{\mathrm{BC}})), \ldots, \mathbf{Obs}_N(\mathbf{x}(\mathbf{u}_{\mathrm{BC}}))]^T \in \mathbb{R}^N$ for ocean state $\mathbf{x}(t, \mathbf{u})$. The second term encodes our a priori knowledge about the atmospheric controls $\mathbf{u}_{\mathrm{BC}}$, penalizing deviations from their first-guess $\mathbf{u}_{\mathrm{BC}}^0$ based on their prior error covariance $\boldsymbol{\Gamma}_{\mathrm{BC}}$. Following general practice, error covariances in Eqn.1 are approximated by their diagonal elements, i.e., their variances (e.g., Wunsch and Heimbach 2007). The gradient obtained by the adjoint model is used to solve $\mathbf{u}_{\min} = \min_{\mathbf{u}_{\mathrm{BC}}} J$ via iterative gradient-based optimization. Following Loose et al. (2020), we assess the relative importance of each atmospheric control in the optimization as follows:

$$||u_{\mathrm{BC}}||^2 = \frac{1}{\sigma_J^2} \sum_{i,j} \left(\frac{\partial J}{\partial u_{\mathrm{BC}}(i,j)} \sigma_{u_{\mathrm{BC}}}(i,j) \right)^2 \in [0,1]. \tag{2}$$

In addition to the surface atmospheric variables currently used in the production of ECCO state estimates, we here include atmospheric pressure in $\mathbf{u}_{\mathrm{BC}}$ (Table 1) which has not been done in previous studies. The indices i, j denote horizontal model grid points and the sum is taken over the full model domain. $\sigma_{u_{\mathrm{BC}}}(i,j)$ comprises the entries of the diagonal matrix $\boldsymbol{\Gamma}_{\mathrm{BC}}$. The sum is normalized by the cost function variance σ_j^2; for example, for BC controls,

$$\sigma_J = \sqrt{[\nabla_{\mathbf{u}_{\mathrm{BC}}} J]^T \, \boldsymbol{\Gamma}_{\mathrm{BC}} \, \nabla_{\mathbf{u}_{\mathrm{BC}}} J},$$

so that the sum of contributions $||u_{\mathrm{BC}}||^2$ across all controls is equal to 1.

b. OSSE forecast model (FM)

Our FM is Release 1 of the Arctic Subpolar gyre sTate Estimate (ASTEr1, Nguyen et al. 2021). The domain covers the Atlantic northward of 32°S, as well as the Arctic and neighboring seas. ASTEr1 is configured on a latitude-longitude-polar cap (LLC) grid with a horizontal resolution

Field	Note
T_{air}	Air temperature
P	Precipitation
R_{sw}	Downward shortwave radiation
R_{lw}	Downward longwave radiation
q_{air}	Specific humidity
u_w	Zonal wind
v_w	Meridional wind
p_{atm}	Atmospheric pressure

TABLE 1. Atmospheric control variables used in this study. Note the addition of p_{atm} compared to the standard set used in ECCO and ASTE.

of $1/3^\circ$ (~22 km in the SPNA), with 50 vertical levels ranging from 10 m at the surface to 450 m at depth. The model allows for ocean mass change via use of a nonlinear free surface (Adcroft et al. 2004) and real freshwater forcing (Campin et al. 2004). ASTEr1 spans the period 2002-2017. It is forced by lateral boundary conditions obtained from the ECCO Version 4 Release 3 (ECCOv4r3, Fukumori et al. 2017) solution and by atmospheric boundary conditions modified from the Japanese 55-year Reanalysis (JRA-55; Kobayashi et al. 2015) during the gradient-based optimization. ASTEr1 applies a constant atmospheric pressure (p_{atm}) loading of $\sim 10^5$ Pa everywhere. Our FM differs from ASTEr1 in applying p_{atm} from JRA-55 and including this variable in the set of control variables (Table 1). This choice is motivated by the strong connection between p_b and p_{atm} on intra-seasonal timescales (Stepanov and Hughes 2006; Na et al. 2016). Its inclusion enables a first assessment of the importance of this new control variable for OBP assimilation within ECCO.

A proposed system of SMART cables within the SPNA used in this study spans 73E to 9W and connects Baffin Bay to the North Sea with a southwest branch reaching Northeastern Canada (Fig. 2). The cables traverse key high-latitude gateways such as the Davis Strait and the Iceland-Faroe Channel, and can potentially provide measurements relevant to monitoring elements of the AMOC. For clarity, we point out that figures and discussion below focus on the SPNA where impacts of assimilation are largest (i.e., a smaller region within the full FM domain is shown in Fig. 2).

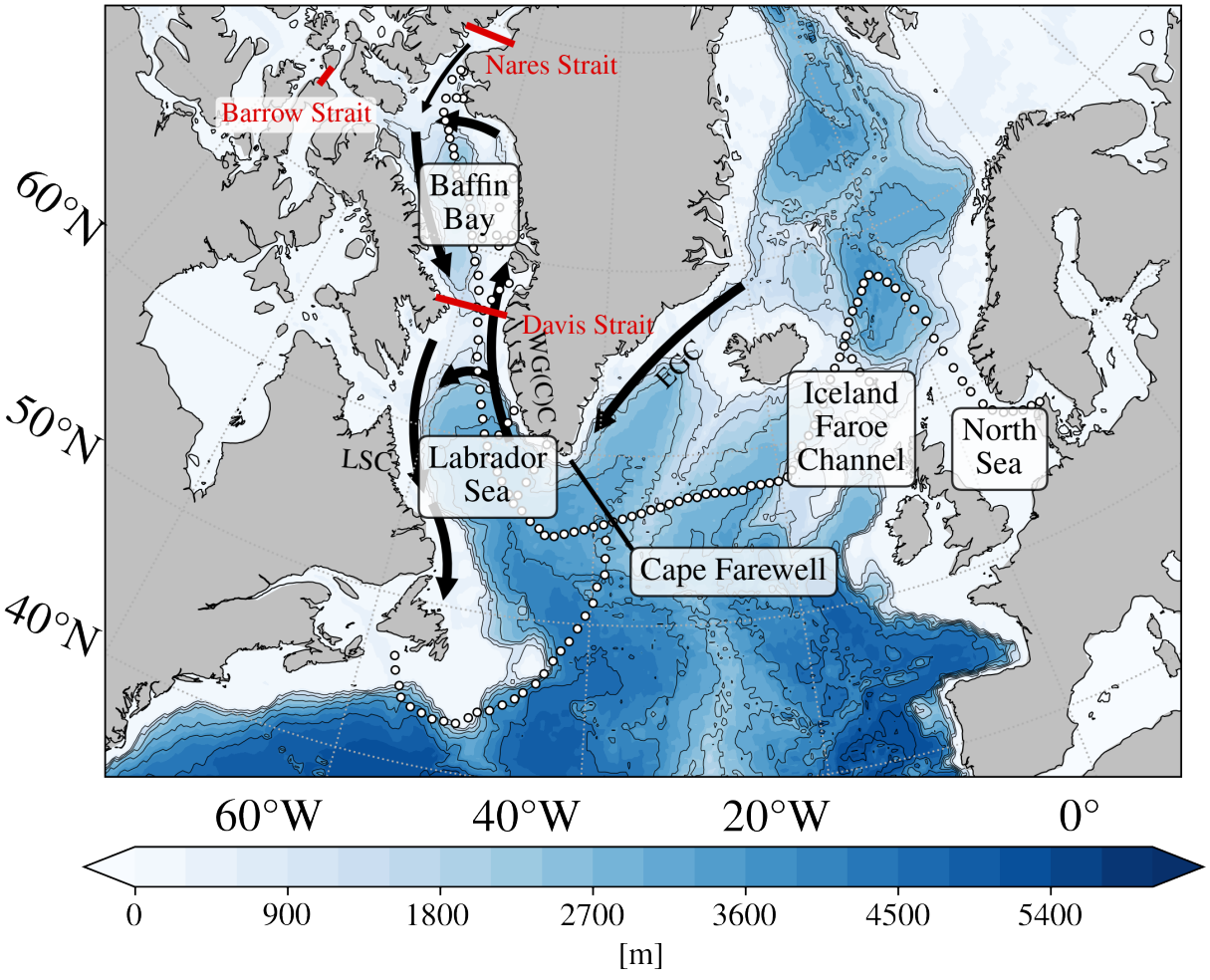

173 FIG. 2. The SPNA region with marginal seas, straits (red lines), and bathymetry (color map and contours).
174 Major currents (black arrows) include the East Greenland Current (EGC), Western Greenland (Coastal) Current,
175 (WG(C)C), and Labrador Sea Current (LSC). White dots indicate sensor locations along the SPNA cable system,
176 spaced approximately 70 km apart, and are points at which synthetic observations will be extracted from the
177 nature run.

185 *c. OSSE nature run (NR)*

186 Our NR is an existing free-running MITgcm simulation (the "LLC4320", Gallmeier et al. 2013;
187 Rocha et al. 2016; Wang et al. 2018; Arbic 2022) configured on the LLC grid at $1/48°$ horizontal
188 resolution with 90 vertical levels ranging from 5 to 500 m thickness. Hourly diagnostics are
189 available for 14 months between September 2011 and November 2012. Key differences between
190 the NR and FM are summarized in Table 2. Importantly, the NR is eddy-resolving (resolution

~2 km in the SPNA), incorporates additional high frequency physics such as tidal forcing (Arbic 2022), and produces submesoscale structures that compare well against satellite data (Gallmeier et al. 2013). Synthetic SMART cable OBP anomalies are extracted from the NR at the locations

	forecast model (ASTE)	nature run (LLC4320)
Domain	Regional (Atlantic + Arctic + Northern North Pacific)	Global
Horizontal grid spacing at equator [degrees]	1/3	1/48
Vertical levels	50	90
Surface level thickness [meters]	5	1
Deep level thickness [meters]	450	500
Atmospheric forcing	3-hourly JRA-55 bulk formulae (Kobayashi et al. 2015) + optimized control adjustments	6-hourly ERA-interim analysis 0.14-degree grid bulk formulae
Atmospheric load	Yes	Yes
Runoff	Monthly mean fluxes based on the R-ArcticNET data set (Lammers et al. 2001; Shiklomanov et al. 2021)	Monthly mean fluxes derived from the GECCO ocean state estimation framework Stammer et al. (2004)
Tides	No	Yes
Barotropic time-stepping	Adams-Bashforth	Crank-Nicolson
Time step [seconds]	1200	25

TABLE 2. Summary of forecast model (FM) and nature run (NR) configurations.

shown in Fig. 2 for assimilation into the FM. We assume a sensor spacing of ~70 km (an anticipated repeater spacing, Howe et al. 2019). Sensor locations are mapped to the nearest neighbor grid point accounting for the irregular LLC grid curvature.

d. Synthetic data processing and uncertainty

Spatial and temporal resolution differences between NR and FM mandate data processing steps. First, the time-mean OBP at each grid cell was removed from the NR's hourly OBP record to eliminate the dynamically unimportant systematic offset arising from differences in local bathymetry between NR and FM. The data were then linearly detrended and detided, removing the sixteen leading tidal constituents, as tides are absent from the FM. Next, monthly means were removed to enable comparison of sub-monthly variability between NR and FM, as the short (14 month) duration of the NR does not allow construction of a monthly climatology. Finally, daily averages were computed from the hourly OBP anomalies, which were then averaged spatially to match the

FM's horizontal resolution (see Table 2). Global synthetic OBP anomalies extracted from the NR output are denoted p_b^{syn}, with those at SMART sensor locations denoted p_b^{SMART}.

In addition to the synthetic data, we require an associated "observational" uncertainty. Since the post-processing steps described above remove many of the signals that would normally contribute to a representation error in the FM, we instead impose a time-invariant uncertainty based on p_b^{syn} variance as follows. We first compute the temporal standard deviation $\sigma_{p_b}(i,j)$ across spatially bin-averaged daily NR p_b^{syn}, and then convert both fields to an equivalent water thickness through multiplication by the scalar constant $1/(g\rho_0)$, where ρ_0 is the constant density 1029 kg m^{-3} and g is the gravitational constant 9.81 m s^{-2}. The derived uncertainty field (Fig. 3) shows high values along the coastal regions due to shallow bathymetry and the heightened influence of small-scale physical processes affecting p_b. Similarly, the high eddy activity in the Gulf Stream give rise to larger transport variability, and in turn higher temporal p_b variability.

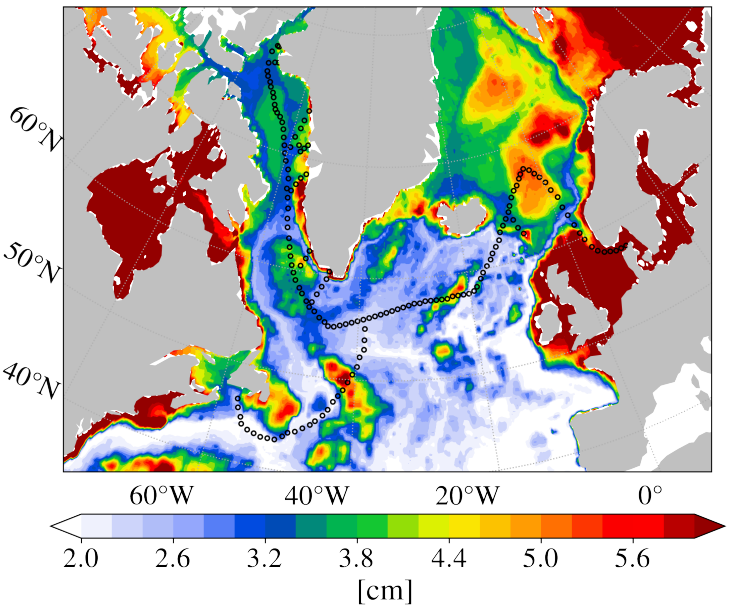

FIG. 3. Synthetic data uncertainty σ_{p_b} used to weight misfits between synthetic NR and FM-derived p_b in equivalent cm of water height. Black circles indicate sensor locations along the SPNA cable system.

The total observation uncertainty $\mathbf{\Gamma}_{\text{obs}}$ is given as the square of the synthetic data uncertainty and instrument errors:

$$\mathbf{\Gamma}_{\text{obs}} = \text{diag}(\sigma_{p_b}^2) + \mathbf{\Gamma}_{\text{instr}}, \tag{3}$$

where $\mathrm{diag}(\sigma^2_{p_b})$ denotes the diagonal matrix whose (n,n) entry is the variance associated with the n-th cable observation. Instrument errors are modeled as independent, zero-mean Gaussian noise with standard deviation 10 Pa (equivalent to 1 mm of water height), consistent with the SMART cable OBP accuracy requirement (JTF Engineering Team 2016). Accordingly, the instrument error covariance is taken to be $\mathbf{\Gamma}_{\mathrm{instr}} = \mathrm{diag}(\sigma^2_{\mathrm{instr}})$ with $\sigma_{\mathrm{instr}} = 10$ Pa, assuming uncorrelated errors. The synthetic data uncertainty in Fig. 3 exceeds the instrument error in magnitude. We seek to reduce the total cost function (Eqn. 1), with the time-dependent p_b misfit contribution defined as

$$J_{\mathrm{misfit}}(\mathbf{s}) = \frac{1}{2}\mathbf{s}^T \mathbf{\Gamma}_{\mathrm{obs}}{}^{-1}\,\mathbf{s}, \tag{4}$$

where

$$\mathbf{s} = \mathbf{S}\left[(\mathbf{y} - \overline{\mathbf{y}}) - \left(\hat{\mathbf{y}} - \overline{\hat{\mathbf{y}}}\right)\right], \tag{5}$$

and with $\overline{\bullet}$ denoting the time-mean over the length of the assimilation experiment, following Fukumori et al. (2017). $\mathbf{S}$ is an isotropic spatial smoother function, which filters out bottom pressure misfit anomaly signals below 300 km. This smoothing focuses on improving the representation of oceanic and atmospheric processes at these scales, rather than addressing potential noisy grid-scale variations (Forget et al. 2015). In the results ahead, we examine the spatial distribution of model-data differences, i.e. the fields that, when squared and summed in space and time, yield J_{misfit}. To this end, we define the "spatial misfit" at fixed time t to be the field given by $\mathbf{s}(\mathbf{x}(t))/\sigma^{1/2}_{\mathrm{obs}}$ where σ_{obs} are the (diagonal) elements of $\mathbf{\Gamma}_{\mathrm{obs}}$.

e. Iterative optimization

Figure 4 provides a high-level summary of our OSSE methodology. An unconstrained FM run serves as "reference" experiment, producing diagnostics ϑ of the model state. Next, synthetic observations sampled from the NR are assimilated into the FM model as described above. No other data (e.g., real observations) are assimilated in our OSSEs. The converged "solution" produces model diagnostics $\tilde{\vartheta}$ along with adjustment fields to the control variables $\mathbf{u}$. A skill score $\mathcal{S}$ measures the improvement in the solution experiment diagnostic as its proximity to the coarse-grained NR, θ^{NR}, relative to the reference experiment via the root-mean-square error (RMSE) as

follows,

$$\mathcal{S}(i,j) = 1 - \frac{\mathrm{RMSE}_t\left(\tilde{\vartheta}(i,j,t), \vartheta^{\mathrm{NR}}(i,j,t)\right)}{\mathrm{RMSE}_t\left(\vartheta(i,j,t), \vartheta^{\mathrm{NR}}(i,j,t)\right)}, \tag{6}$$

where RMSE_t denotes the RMSE computed along the time dimension at each horizontal model grid point (i,j), as we examine improvement to selected 2D time varying fields in this study.

In the 2D skill map, a positive skill score indicates a more accurate solution than the reference experiment. For example, a skill of 0.1 indicates a modest but positive improvement in the solution's representation of ϑ's variability, reflecting a 10% reduction in RMSE relative to the reference state. Equivalently, positive skill can be understood as an increase in explained variance (see Appendix A1).

When assimilating synthetic observation anomalies, the cost function targets the quantity's *variability* rather than its full state. Because anomalies are defined by removing each run's own time-mean, the time-mean difference between solution and reference anomalies is identically zero and therefore cannot be used to assess mean-state improvement. To quantify systematic changes, we instead diagnose the time-mean difference in the *full* bottom pressure, P_b. At each grid point (i,j), we define

$$\delta P_b(i,j) = \overline{\widetilde{P_b}(i,j,t) - P_b(i,j,t)}, \tag{7}$$

where again $\tilde{\bullet}$ denotes the constrained OBP and $\overline{\bullet}$ denotes the time-mean. We will refer to $\delta P_b(i,j)$ as the "mean adjustment".

Our set of 14 OSSEs is described in Table 3. In each set, first guess adjustments for all controls (Table 1) except p_{atm} are initialized from ASTEr1 and interpolated to daily frequency from their original biweekly frequency. Control uncertainties $\sigma_{\mathbf{u}}$ are identical to those used in ASTEr1. For p_{atm}, first guess adjustments are zero and uncertainties are estimated from the standard deviation of daily-mean values from JRA-55 for the year 2012. Given that this is the first application of p_{atm} as a control in the state estimation framework, we impose no penalty on deviations from the first guess, i.e., $\mathbf{\Gamma}_{\mathrm{BC}}^{-1}$ for p_{atm} is set to zero in J_{BC} in Eqn. 1. The control adjustment frequency is discussed further in Section 4.

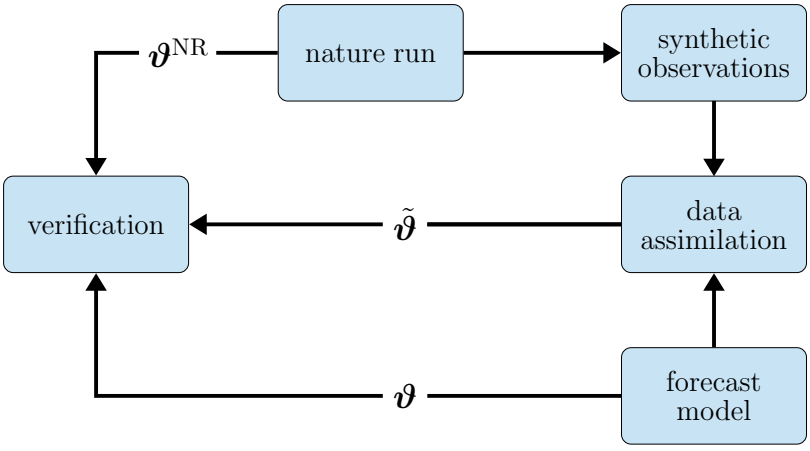

FIG. 4. OSSE flowchart adapted from Hoffman and Atlas (2015). Synthetic observations from the NR are assimilated into the FM. Solution and reference experiment fields $\tilde{\vartheta}$ and ϑ, respectively, are verified against the analogous NR output ϑ^{NR} using a skill score (Equation 6).

Expt. number & name	Run Time	Aim	Iterations	Notes
1. SPNA_cable	Jan 2012	Assess daily OBP data value from the SPNA cable	20	
2. LS_cable 3. SPG_cable 4. NS_cable 5. Nfl_cable	Jan 2012	Explore spatial origins of daily OBP data value in expt. SPNA_cable.	20	OSSEs assimilating data from the (LS) Labrador Sea, (SPG) subpolar gyre, (NS) North Sea, and (Nfl) Newfoundland segments of the full SPNA cable (Fig. 1). Expt. LS_cable also re-run with p_{atm} control excluded
6. SPNA_cable_annual 7. GRACE_annual	Jan–Dec 2012	Explore complementarity of daily OBP data from SPNA cable with monthly global OBP data from GRACE	3	GRACE_annual targets minimization of monthly OBP misfits.
8-14. SPNA_cable_adjfreq_[1:0.5:4]	1–7 Jan 2012	Explore dependence of dominant control on imposed adjustment frequency	20	Misfit computed only during final 2 days. In expt. name, number given in brackets denotes control adjustment frequency in days. For example, expt. SPNA_cable_adjfreq_4 adjusts controls every 4 days.

TABLE 3. Summary of OSSE configurations. Horizontal dashed lines group experiments by aim. Experiments 2-5 are referred to in the text as the "partial cable" OSSEs. Unless otherwise stated, all OSSEs are run with the full set of controls listed in Table 1 and target minimization of daily OBP misfits over the full run time.

3. Results

All results below are shown for the final iteration of the optimization for each OSSE (Table 3). We start by describing the results from the full SPNA_cable OSSE, run for the month of January 2012 to test the impacts of assimilating daily p_b^{SMART} data at all sensor locations shown in Fig. 2.

a. Impact on bottom pressure and barotropic velocity

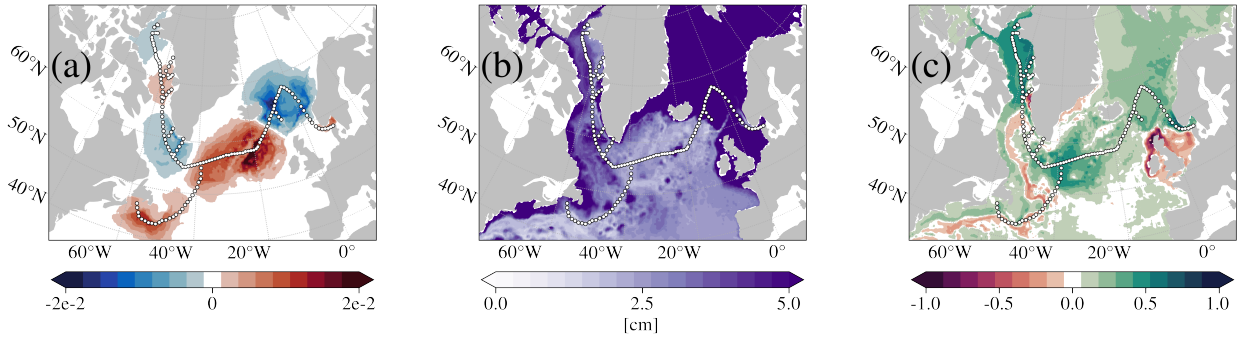

FIG. 5. (a) Normalized p_b spatial misfit on January 1, 2012, (b) RMSE between $\tilde{p}_b$ and p_b^{NR}, and (c) p_b skill in the SPNA cable experiment.

Figure 5a shows the spatial p_b misfit remaining on January 1, 2012 in the SPNA_cable OSSE at the end of the iterative optimization. Spatial misfits on subsequent days (not shown) are qualitatively comparable, with positive and negative signals extending away from the sensor locations due to the application of the spatial smoother (Eq. 5). The cost has been reduced by 83% and the final RMSE is shown in Fig. 5b. Owing to high p_b variability, the FM and NR show largest differences in p_b in shallow coastal waters and semi-enclosed regions, including the North Sea, Hudson Bay, and Canadian Arctic Archipelago. The skill score ($\mathcal{S}$, Eqn. 6) distribution in Fig. 5c indicates significant p_b error reduction both along the cable and throughout the wider SPNA region, extending into the Greenland, Iceland, and Norwegian Seas, with p_b error increases in only a few isolated areas.

To explore regional origins of the improved skill (Fig. 5c), we conduct four additional partial cable OSSEs (LS_cable, SPG_cable, NS_cable, and Nfl_cable, Table 3). Each partial cable OSSE assimilates p_b^{SMART} for one of the cable segments shown in Fig 1. Skill scores for these OSSEs are shown in Fig. 6. Depending on the cable segment assimilated, certain regions, such as the Subpolar Gyre, Baffin Bay, and northern North Sea, exhibit similarly high p_b skill (Fig. 6a-d) as the full cable experiment (Fig. 5c). We note that spatial misfits in the full cable experiment (SPNA_cable) cannot be recovered from the sum of the four partial cable experiment misfits due to the application of the spatial smoothing (Eqn. 5). This also explains why some impacts of full cable assimilation

(e.g., reduced skill in the North American continental slope and southern North Sea shown in Fig. 5c) are not seen in any of the partial cable experiments (Fig. 6a-d).

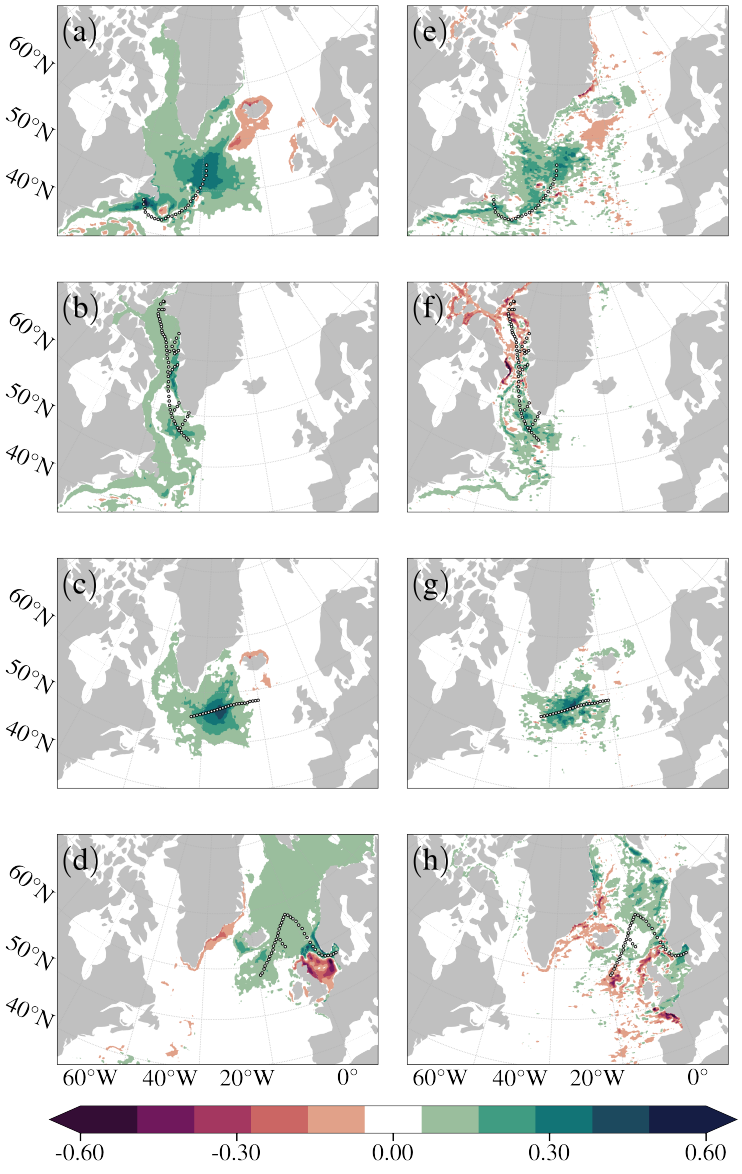

FIG. 6. (a-d) p_b and (e-h) meridional barotropic velocity skill scores for the four January 2012 daily-control partial cable experiments. The zonal barotropic velocity skill scores (not shown) resemble their meridional counterparts.

Having demonstrated that OBP assimilation improves OBP representation at both the sensor locations and throughout the wider SPNA, we now inspect impacts on other QoIs in the partial cable OSSEs. We start by examining the response of the barotropic (depth-integrated) velocity,

anticipating improvements due to its linear relation to OBP where geostrophy holds. The skill score (Eqn. 6) for the daily meridional barotropic velocity, V_{bt}, is shown in Fig. 6e-h. Skill scores for the zonal component, U_{bt}, are not shown but are quantitatively comparable. Skill patterns for V_{bt} (Fig. 6e-h) and p_b (Fig. 6a-d), show strong similarity due to their dynamical connection (i.e., sensitivity to the same atmospheric forcings and subject to the same resulting oceanic adjustments). In addition to demonstrating the expected relationship between water-column mass and depth-integrated velocity, the results shown in Fig. 6 highlights the benefit SMART provides towards indirectly constraining large-scale SPNA circulation upon assimilation.

b. Impact on Advective freshwater flux

We now investigate assimilation impacts on freshwater exports from the Arctic, which are difficult to constrain via direct observations. These exports are rapidly evolving due to anthropogenic intensification of the hydrological cycle (Douville et al. 2021), changing sea ice extent (Serreze and Meier 2019) and river runoff (Weiss-Gibbons et al. 2024), increased Greenland Ice Sheet melt and calving (King et al. 2020), and shifts in regional export pathways (Zhang et al. 2021; Zhang and Du 2025), with potentially significant downstream impacts on the AMOC (Haine 2020). We focus on two primary routes through which Arctic freshwater (FW) reaches the SPNA (Jahn et al. 2010; Haine et al. 2015). The first pathway is through Fram Strait, where FW is transported southward by the East Greenland Current (EGC, Fig. 2). After rounding Cape Farewell the current bifurcates: one branch, the West Greenland Current (WGC), continues westward into the Labrador Sea joining the Labrador Sea Current (LSC), while the other, the West Greenland Coastal Current (WGCC) turns northward through Davis Strait into Baffin Bay (Pacini and Pickart 2022). The second pathway delivers Arctic FW through narrow passages in the Canadian Arctic Archipelago (CAA) including the Nares and Barrow Straits. Along this path, sea ice travels southward along the western coast of Baffin Bay and exits through Davis Strait, joining the LSC (Münchow and Melling 2008).

To investigate the ability of SMART observations to constrain these transports, we examine assimilation impacts in the Labrador Sea cable experiment (LS_cable, Table 3). The connection between the SMART OBP constraints and FW transports are explained in terms of the optimization's implied impacts on the wind-driven circulation as depicted in Fig. 7. All SMART sensors

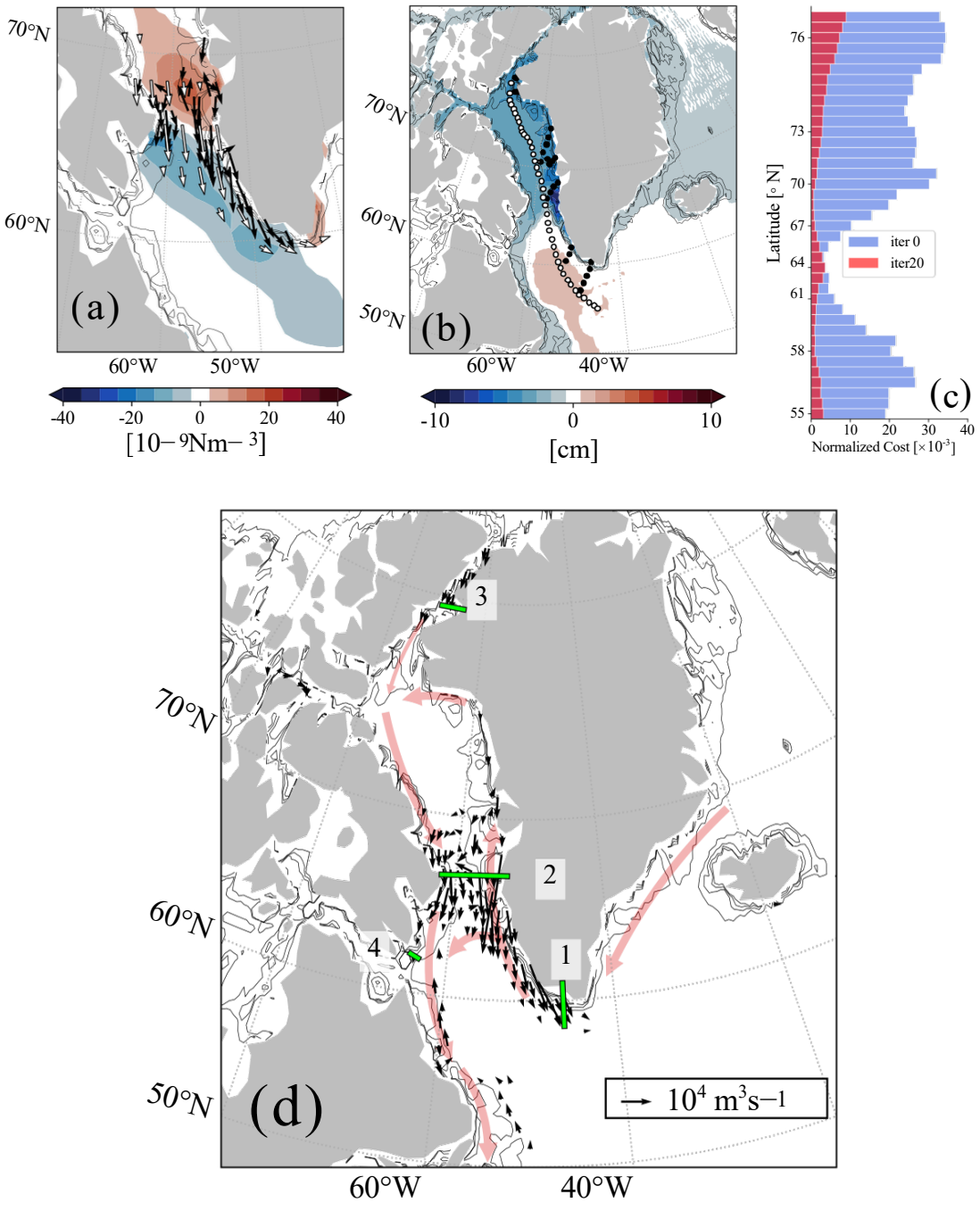

FIG. 7. (a) January mean wind (white arrows) and sea surface (black arrows) velocity adjustments, with wind stress curl adjustment shown in blue and red shadings. (b) The January mean P_b adjustment (Eqn. 7) in equivalent units of height, with the Labrador Sea cable indicated by dots. White dots highlight the central vein's sensors, for which a histogram illustrates the p_b misfit reduction in (c). January mean advective surface FW flux adjustment is shown in (d) with SPNA circulation indicated by red arrows. Green lines mark gateways across which the meridional component of $\mathrm{ADV}_{\mathrm{fw}}$ skill is assessed (Table 4). Black contours show geostrophic f/H isolines.

along the cable's central vein (filled white in Fig. 7b) exhibit a reduction in p_b misfit at the end of the optimization, as shown in the histogram (Fig. 7c). From the January mean adjustment made to the winds (white arrows in Fig. 7a), we compute a wind stress curl adjustment featuring a dipole centered just south of Davis Strait. A positive curl (red) over Baffin Bay and a negative curl (blue) over the Labrador Sea induce Ekman transport anomalies (black arrows in Fig. 7a) with cyclonic flow and surface divergence across the Davis Strait. This leads to a local decrease in January mean sea surface height and P_b (Eqn. 7), the latter of which is shown in Fig. 7b. The northward WGCC decreases due to the southward surface current adjustment. Ekman transport in response to the wind adjustments (Fig. 7a) deflects these coastal current adjustments west, which shifts water mass away from the coast and into the Labrador Sea, leading to a P_b increase in the Labrador Sea interior (Fig. 7b). The negative coastal OBP adjustment is associated with the propagation of coastally trapped barotropic waves following f/H contours (e.g., Chen et al. 2023). This mechanism is demonstrated in detail through SPNA and Arctic surface wind perturbation experiments in Fukumori et al. (2015).

The coastally trapped wave adjustments impact the FM representation of advective FW transport, $\mathrm{ADV_{fw}}$, as exemplified by the January mean adjustment following Eqn. 7 and depicted in Fig. 7d. $\mathrm{ADV_{fw}}$ is computed component-wise, e.g. the meridional component is computed by vertically integrating the meridional volume transport multiplied by the freshwater fraction relative to reference salinity 34.8 psu. The time-mean surface circulation pathways in the FM are illustrated in red. Assimilation results in a decrease in the EGC rounding Cape Farewell (gate #1, Fig. 7d) and the northward WGCC, reducing FW transport toward the Davis Strait (gate #2). Concurrently, southward FW export from the Arctic through Nares Strait (gate #3) intensifies and travels south along the western Baffin Bay coast. The increased southward FW export continues through Davis Strait to the Labrador Shelf (gate #4).

The $\mathrm{ADV_{fw}}$ adjustments are verified against the NR at the four gates (Table 4). As above, the meridional $\mathrm{ADV_{fw}}$ skill is a 2D field expressing error reduction (Eqn. 6). To quantify skill at each gateway, we sum this field along model grid cells spanning the gateway section. A net reduction in meridional $\mathrm{ADV_{fw}}$ error is found at all gateways except for Nares Strait, indicating that, for the most part, assimilating p_b from the Labrador Sea cable improves representation of large-scale freshwater redistribution in the SPNA. We confirm that the adjustment of the wind

controls dominates ADV_{fw} improvements by repeating the OSSEs with the p_{atm} control (which dominates OBP misfit reduction) disabled. We find quantitatively comparable velocity adjustments and ADV_{fw} skill to those presented here.

	Gateway	ADV_{fw} skill %
1	Cape Farewell	4.04
2	Davis Strait	10.07
3	Nares Strait	-4.12
4	West Labrador Sea	5.35

TABLE 4. Skill of the meridional component of surface advective FW transport (ADV_{fw}) anomaly for gateways shown in Fig. 7d.

c. Impact of assimilating GRACE versus SMART data on annual state estimates

We conduct a final pair of OSSEs spanning the year 2012 to demonstrate how SMART's daily pointwise p_b observations may complement monthly global p_b products from GRACE (or GRACE-FO) due to their distinct temporal and spatial sampling patterns. In the first (experiment SPNA_cable_annual, Table 3) we repeat the full SPNA cable OSSE using daily SMART cable data (as in Section 3a) only this time for the full year 2012. In the second (experiment GRACE_annual, Table 3) we assimilate synthetic monthly "GRACE" data, denoted as p_b^{GRACE}, into the FM, which is sampled from the NR for the full year 2012 as described in Appendix C1. Due to the computational burden of the year-long NR integration, these final two OSSEs are run for short optimization cycles (only 3 iterations). We anticipate that further optimization would not lead to strong qualitative alteration of our results, however, as in all previous OSSEs run (Table 3), skill evolution over successive iterations is characterized by a standing pattern of amplification to first order (see Supplementary Information).

For both of these annual OSSEs, skill scores are computed from monthly average fields. As in the January SPNA cable OSSE (SPNA_cable, Section 3a), high skill in SPNA_cable_annual is concentrated around the shallow cable endpoints, where smoothed spatial misfits are large. These areas include Baffin Bay, Grand Banks and the North Sea. Over the full year, we find lower misfits in the Subpolar Gyre compared to the January experiment (Fig 5). Consequently, the Subpolar Gyre skill is lower for experiment SPNA_cable_annual (Fig. 8a). As above, Fig. 8a indicates barotropic propagation of the assimilated constraint, with improvement in skill spreading away from the cable

location along f/H contours. This is consistent with Jones et al. (2018) (their Fig. 10) and Loose et al. (2020) (Supporting Information Movie S7) who map the fast barotropic pathways connecting the Greenland-Iceland-Scotland ridge and the Labrador Sea along f/H contours on timesecales of 2-3 weeks.

In contrast to the SPNA_cable_annual OSSE, targeted misfit reductions (spatial misfits not shown) are not confined to the Greenland-Iceland-Scotland seas in the GRACE_annual OSSE but spread more uniformly through the North Atlantic due to the global coverage of GRACE p_b estimates. As a result, SPNA p_b skill in GRACE_annual (Fig. 8b) is broadly positive, but generally lower in magnitude than in SPNA_cable_annual. Significant negative p_b skill (i.e., worsened representation of NR variability) is seen in the Gulf Stream region in both annual OSSEs. In this highly eddying region, misfit reduction is likely complicated by spatial smoothing and limited control adjustment frequency in the optimization procedure.

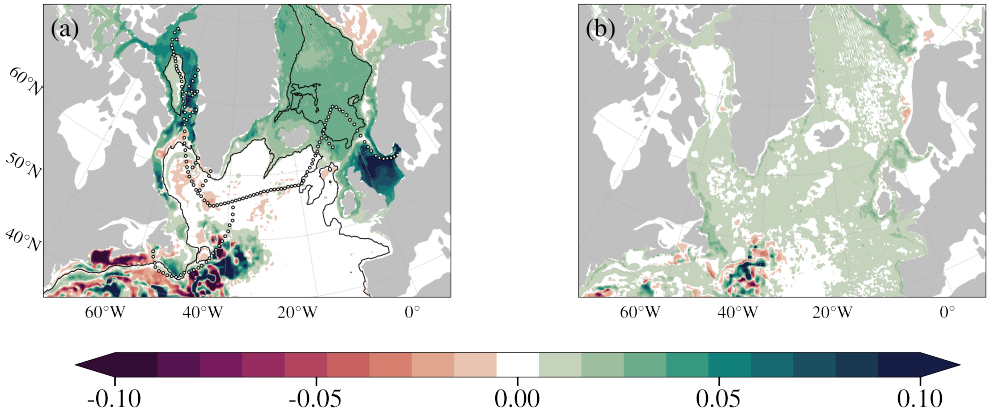

FIG. 8. Comparison between 2012 monthly p_b skill attained by assimilating (a) daily synthetic SMART cable data in experiment SPNA_cable_annual and (b) monthly synthetic GRACE data in experiment GRACE_annual.

4. Discussion

We have shown that synthetic SMART OBP data may improve skill in observed (i.e., collocated OBP) and unobserved quantities (e.g., remote OBP as well as derived quantities such as freshwater transports in the subpolar North Atlantic). To understand how the optimization achieves improved skill, we now examine how the atmospheric control variables are adjusted as part of the model-data misfit reduction and the way in which they incur circulation improvements. By performing this

investigation within the partial cable OSSEs (see Fig. 6) we provide an in-depth understanding of the impact of SMART sensors on the state estimate and how skill improvements are achieved.

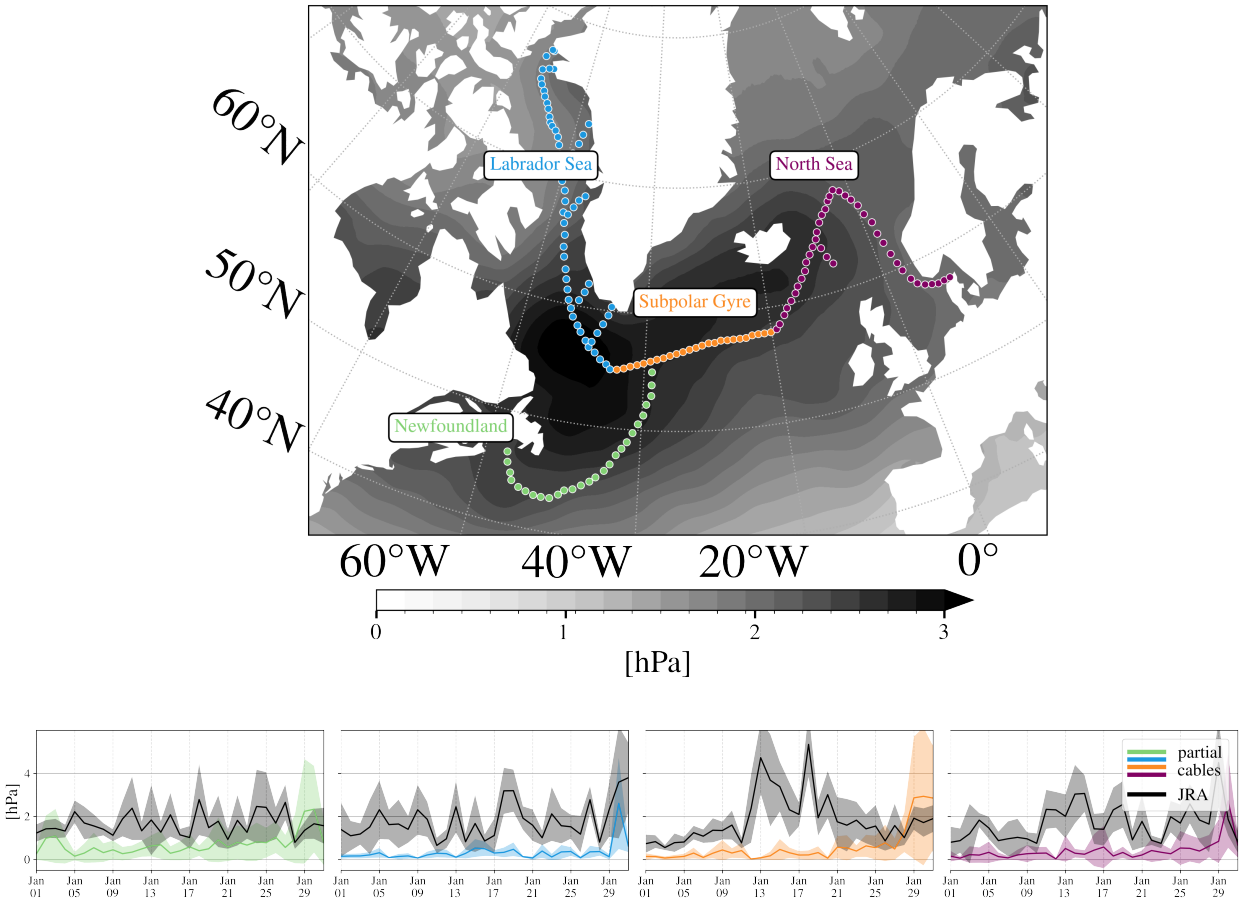

FIG. 9. (Top) Standard deviation of daily JRA-55 surface pressure, averaged over 2012, with the locations of the 4 cable segments used in the partial cable OSSEs shown in color. (Bottom) Black curves show daily JRA-55 standard deviations, with grey envelopes indicating sub-daily variability (standard deviation computed from 3-hourly records). Colored curves show mean absolute value of p_{atm} adjustments in the four partial cable January OSSEs with standard deviations shaded. Each time series is computed as an average across all sensors in a given partial cable.

In every OSSE, p_{atm} dominates the optimization's control adjustments, contributing around 98% to the misfit reduction (determined using Eqn. 2). Since we do not penalize control deviations from first guess values, there is a risk that the optimization will employ excessive adjustments to force misfit reduction. As such, it is instructive to compare p_{atm} adjustment magnitudes against typical variations of p_{atm} of the reanalysis. Figure 9 (top) shows the average standard deviation

of daily p_{atm} from the JRA-55 reanalysis product for the year 2012, which was used to construct the control uncertainties applied in our OSSEs (σ_u, Section 2a). These amplitudes are consistent with p_{atm} uncertainty estimates from Ponte and Dorandeu (2003), based on the spread between atmospheric reanalyses. In Fig. 9 (bottom), time series of p_{atm} adjustments (colored) are compared to p_{atm} variability in JRA-55 (black) for the partial cable OSSEs. All time series are computed as an average across all sensors in a given cable, with the relevant JRA-55 values selected via nearest neighbor interpolation. In general, p_{atm} adjustments are much smaller than p_{atm} variability estimated in JRA-55 and are therefore well within acceptable uncertainty bounds; no extreme atmospheric pressure adjustments are made to overfit the model to the observations. To check if our results are highly sensitive to our choice of specified control uncertainty, we re-ran experiment SPNA_cable defining σ_u from atmospheric reanalysis spread following Chaudhuri et al. (2014) and found no notable impact on p_{atm} adjustments or OBP skill (Appendix B1).

Next, we seek an understanding of the spatial pattern of the atmospheric pressure adjustment that was inferred to reduce the model-data misfit. Taking experiment SPNA_cable as an example, we inspect how the initial p_b spatial misfit pattern (Fig. 10a) is reduced over 20 iterations of optimization to leave a residual spatial misfit pattern (Fig. 10b). The misfit reduction is achieved by an adjustment of p_{atm} (Fig. 10c), which acts to increase loading over the regions of positive misfit, and vice versa for regions of negative misfit. The p_{atm} adjustments are spatially extended relative to the spatial misfit, due both to smoothing (Section 2d) and oceanic teleconnections propagating the influence of assimilated p_b away from the cable over the OSSE duration. The standard deviation of p_{atm} adjustments divided by the JRA-55 uncertainty field from Fig 9 is shown in Fig. 10d to be no more than about 50%, reaffirming that the adjustments are reasonable.

The adjustments shown in Fig. 10 reflect the isostatic response of sea level to atmospheric pressure loading, i.e., the inverse barometer (IB) effect. As atmospheric pressure decreases, sea level rises locally, and vice versa. On timescales of several days and longer these changes largely compensate, leading to small net changes in p_b (Ponte 1992). On shorter timescales - relevant in our SMART OSSEs due to the use of daily control adjustment frequencies - p_b variations are larger due to insufficient time for a complete IB response to be achieved via barotropic wave adjustments. In Fig. 10 the result of this partial IB response is seen, with (Fig. 10c) daily p_{atm} adjustments being

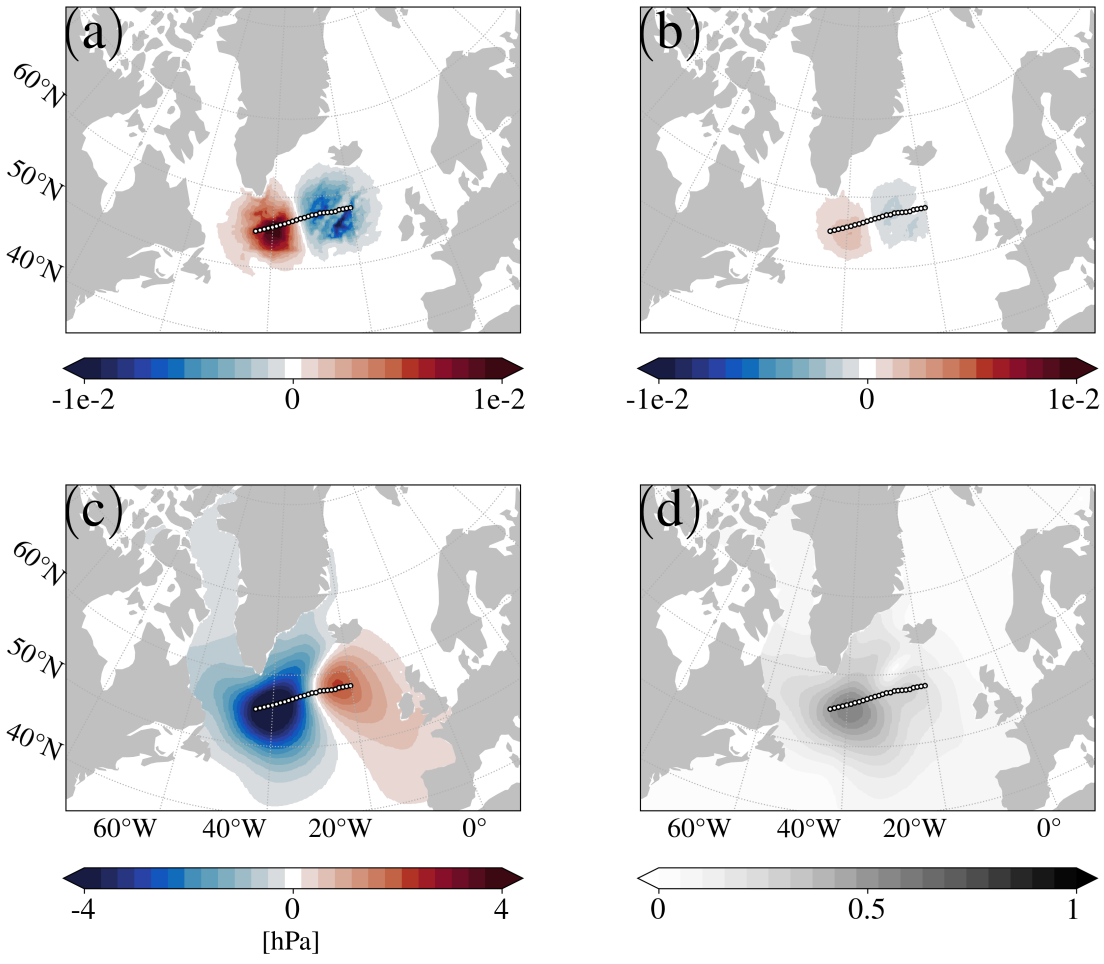

FIG. 10. (a) A smoothed and normalized p_b spatial misfit along the Subpolar Gyre cable taken from one day of the January OSSE after (a) 0 and (b) 20 optimization iterations. Misfit reduction is achieved by (c) an opposite-signed adjustment to p_{atm}, shown for the same day as (a,b). (d) Standard deviation of p_{atm} adjustments taken across all days of the month normalized by the JRA-55 uncertainty field from Fig 9.

transmitted to the seafloor (Fig. 10b) before changes in atmospheric loading are offset by the local sea level response.

Whilst all of our OSSEs are dominated by adjustments of the atmospheric pressure control, surface wind adjustments play an important secondary role in misfit reduction. Specifically, Ekman pumping and suction can drive changes in bottom pressure anomaly when the response is predominately barotropic, as was demonstrated on seasonal timescales in Chen et al. (2023). Despite p_{atm} dominating the OBP-driven optimization, we found that it is the wind adjustments that effectively excited variability in our freshwater transport QoIs. This apparent contrast reflects

a distinction between the mechanisms that reduce OBP misfit and those that drive dynamically relevant circulation changes. Atmospheric pressure adjustments provide an efficient means of fitting OBP through the inverse barometer response, but do not substantially alter adjustments to freshwater transport. This separation is consistent with prior work emphasizing the importance of wind-driven, nonlocal dynamics in shaping bottom pressure variability (Ponte, 1994). Consistent with this interpretation, we find that comparable improvements in OBP skill and freshwater transport can be obtained in experiments that exclude atmospheric pressure as an active control (not shown), indicating a degree of non-uniqueness in the attribution of OBP variability within the inverse framework.

The relative importance of different controls for both misfit reduction and QoI response depends upon many choices made in configuring our OSSEs, including specified control frequency and time lag between control adjustment and misfit/QoI evaluation. To demonstrate this, we perform a final set of seven OSSEs (experiments 8-14 in Table 3) that are identical to SPNA_cable, except that the integration time is reduced to 7 days, daily p_b^{SMART} observations are assimilated on the final two days only, and the control adjustment frequency is varied. As for SPNA_cable, all atmospheric controls from Table 1 are active. The rationale for computing the misfit only at the end of the runs is to investigate the lag between the control adjustment and misfit evaluation, and to expose different timescales underpinning the wind- and pressure-driven adjustments influential in our OSSEs. Fig. 11 shows that for control adjustment frequencies exceeding 3 days, the winds overtake atmospheric pressure as the dominant control on OBP variability, consistent with Ponte (1994). On these timescales OBP sensitivities to atmospheric pressure weaken as barotropic adjustments accomplish a complete IB response. On shorter timescales (e.g., the daily timescales considered in our previous OSSEs listed in Table 3) atmospheric pressure variations imprint on OBP, dominating OBP variability and misfit reduction.

Both the ASTEr1 and ECCO global solutions use biweekly atmospheric control adjustments to reduce misfits to data assimilated over a wide range of frequencies (e.g., including daily and long-term climatologies). In this study, we found daily control adjustments to be critical for best extracting the information from daily data to improve FM skill. When using biweekly control adjustments (not shown), cost reductions are achieved but accompanied by degraded skill in many regions, owing to the definition of skill in terms of time series from daily data and the

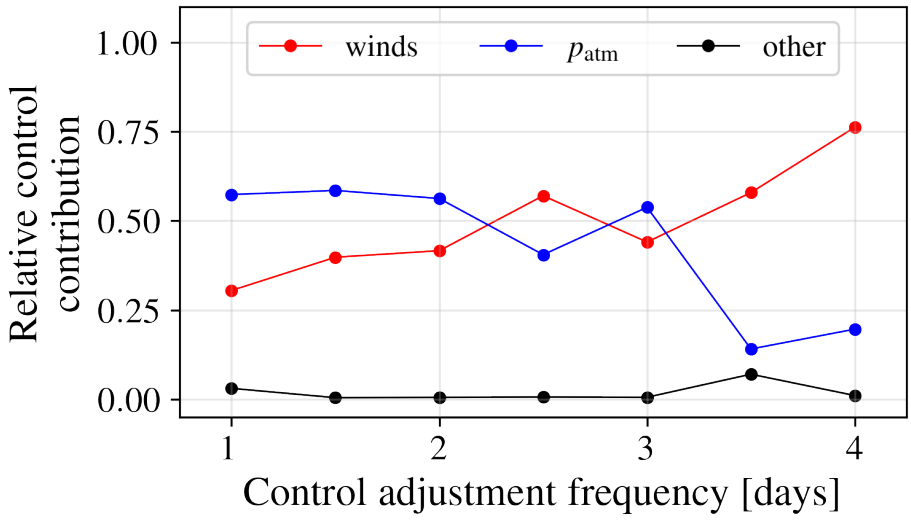

FIG. 11. Relative contributions of (red) wind, (blue) atmospheric pressure and (black) other controls listed in Table 1 as a function of control adjustment frequency which was varied across the final 7 OSSEs in our ensemble (experiments SPNA_cable_adjfreq_[1:0.5:4] plotted here and described in Table 3). Control contributions are computed via Eqn. (2).

limited integration period of one month. Since atmospheric forcing adjustments cannot strongly influence ocean variations at frequencies exceeding the adjustment frequency, care must be taken in formulating the optimization to fully leverage available observational constraints.

5. Conclusions and Outlook

In this study, we conducted an ensemble of observing system simulation experiments (OSSEs) in the ECCO state estimation framework to evaluate the potential of the SMART subsea cable observing system to constrain ocean bottom pressure and additional climate-relevant quantities of interest in the subpolar North Atlantic (SPNA). SMART has emerged over the last decade as a proposed global initiative to leverage commercial subsea telecommunications cables for real-time geophysical observations, including ocean bottom pressure, temperature, and seismic activity. In situ ocean bottom pressure measurements remain sparse yet critically important for understanding ocean mass redistribution and large-scale circulation. The proposed SMART cable route across the SPNA presents a unique opportunity to fill a niche in this climatically sensitive region by

providing continuous, high-frequency, vertically integrated mass measurements unavailable from existing networks.

The motivation for our OSSEs stems from the desire to quantify how SMART data could enhance ocean state estimation prior to cable deployment. To our knowledge, this work is the first published, detailed OSSE-based investigation into the impact of SMART observations on the ocean observing system. It builds on one previous unpublished study (Tobias Weber, private communication) demonstrating OBP error reduction when assimilating synthetic SMART observations obtained from the Max Planck Institute Ocean Model. In contrast to their ensemble Kalman filter data assimilation approach, we use the dynamically and kinematically consistent adjoint method for assimilation. An added benefit of our approach is that it enables a detailed investigation into the physical mechanisms underlying SMART p_b impacts on both local and remote quantities of interest that are not directly observed.

As an expected result, we found that assimilation of (synthetic) p_b observations improves the representation of simulated p_b variability. The improvement is widespread, but strongest local to the cable. Importantly, beyond this direct effect, improvements were also demonstrated in unobserved, state-derived quantities of interest (QoI). We focused on two such QoIs which are closely related to the large-scale circulation. First, SMART's constraint on p_b was found to increase explained variance in barotropic velocities. Second, an improved representation of advective freshwater transports from the Arctic to the North Atlantic subpolar gyre was demonstrated, quantified in terms of improved skill across three out of four gateways. These examples underscore that SMART's contribution to the global ocean observing system will extend beyond the quantities directly monitored. Additionally, our results demonstrate the value SMART may add to GRACE OBP monitoring, with SMART providing substantial oceanic mass distribution constraints along particular barotropically connected pathways in the North Atlantic, complementing GRACE's spatially more homogenous skill improvement..

The optimization was largely governed by surface atmospheric pressure adjustments, reflecting the inverse barometer response that dominates p_b variability on short timescales, while wind-driven adjustments become more important at longer timescales. We found that the benefit of daily SMART observations is only fully realized when control updates are applied at comparable

frequency; biweekly updates, as in current ECCO practice, reduce p_b skill and can degrade performance due to temporal aliasing.

While our results are encouraging, all OSSEs in our ensemble were limited to run times of one year or less. Since SMART offers a pathway for sustained, long-term OBP monitoring, future work should interrogate SMART's value for constraining ocean variability on seasonal to decadal time scales in extended OSSEs when suitable NR outputs become available. In the ECCO framework, this extension could also include longer lead times prior to data acquisition to interrogate the potential of future SMART networks to constrain the historic ocean state. Importantly, all extended OSSEs should incorporate realistic modeling of time-evolving sensor performance, such as the linear-plus-exponential formulation introduced by Hughes et al. (2012), to explicitly account for bottom pressure sensor drift.

Recent advances deploying Hessian uncertainty quantification (Loose et al. 2020; Loose and Heimbach 2021) could also be leveraged to rigorously quantify the complementarity of SMART observations with existing satellite (e.g., GRACE) and in-situ networks. Additionally, we note that our OSSEs were conducted for optimization cycles of 20 iterations or less. Whilst we suggest further iteration would have limited qualitative impact on our results, quantitative impacts could be investigated in future work. Finally, our choice of synthetic data uncertainty incorporated variability that should be recoverable by the FM. This may have served to downweight the strength of the assimilated OBP constraint in the state estimation framework, encouraging investigation of alternate uncertainty estimates in future work. Within an operational or production-type data assimilation framework, improving uncertainty estimates is an iterative process that involves analysis of residual errors or posterior uncertainties. Such analysis often points to the need for improving the uncertainty estimates, including representation errors and prior uncertainties in the control variables.

The design of the SPNA SMART network is still evolving. While cable routing and sensor types will not be dictated by science requirements, questions remain about optimal sensor spacing (see Appendix D1), placement on continental shelves versus abyssal plains, and the number of observation points needed to maximize impact. OSSEs could help inform these design questions. Our study establishes a methodological foundation for evaluating the unique contribution of SMART cables to the global ocean observing system. Results shown encourage future assessment of both the potential constraint SPNA SMART offers on AMOC and the complementarity between SPNA

SMART and existing observing networks in the region (e.g., the OSNAP Array (Lozier et al. 2017), long-term moorings (Handmann et al. 2018; Mercier et al. 2024; Curry et al. 2014), and tomographic arrays (Avsic et al. 2005). In particular, there is growing interest within the AMOC observing community in using improved OBP constraints to assess reference level velocity assumptions in geostrophic shear calculation (Foukal et al. 2026). In addition, SMART temperature sensors have the potential to provide sustained, high-resolution measurements of bottom boundary layer processes, which are important for examining turbulence and mixing and closing regional and global heat budgets. Future experiments should also investigate SMART acoustic sensing of sound speed along ray paths to obtain absolute water velocity along cables. These findings may further bolster SMART's position as a transformative component of the ocean observing system, offering novel insights on dynamics that are otherwise difficult to obtain.

APPENDIX A

A1. Relationship between RMSE and explained variance

Explained variance, defined

$$\mathrm{EV}(x,y) = 1 - \frac{\mathrm{Var}(x-y)}{\mathrm{Var}(x)} \tag{A1}$$

quantifies the extent to which one variable explains another (Fukumori et al. 2015). That is, EV is closer to 100% the more y accounts for variability in x. Consider one-dimensional zero-mean random variables x, y, and z (e.g. time-series of climate anomalies). Without loss of generality, the variance of such a variable is

$$\mathrm{Var}(x) = \mathbb{E}[x^2].$$

Next, with root-mean squared error defined $\mathrm{RMSE}(x,y) = \mathbb{E}[(x-y)^2]^{1/2}$, it follows that

$$\mathrm{RMSE}(x,y) = (\mathrm{Var}(x-y))^{1/2}.$$

Substituting into Equation (A1), we write the explained variance for mean-zero variables as

$$\mathrm{EV}(x,y) = 1 - \frac{\mathrm{RMSE}(x,y)^2}{\mathrm{Var}(x)}. \tag{A2}$$

The denominator $\mathrm{Var}(x)$ is fixed and nonnegative, so clearly a decrease in $\mathrm{RMSE}(x, y)$ increases $\mathrm{EV}(x, y)$. Recalling the definition of skill introduced in Equation 6, we have

$$S = 1 - \frac{\mathrm{RMSE}(x, y)}{\mathrm{RMSE}(x, z)} = 1 - \frac{(\mathrm{Var}(x - y))^{1/2}}{(\mathrm{Var}(x - z))^{1/2}}.$$

Therefore, in the event that the set $\{x, y, z\}$ attains positive skill, $S > 0$ implies

$$(\mathrm{Var}(x - y))^{1/2} < (\mathrm{Var}(x - z))^{1/2}$$
$$\mathrm{Var}(x)\,[1 - \mathrm{EV}(x, y)] < \mathrm{Var}(x)\,[1 - \mathrm{EV}(x, z)]$$
$$\mathrm{EV}(x, y) > \mathrm{EV}(x, z)$$

invoking Equation A1. In the context of an OSSE involving anomaly fields $\{\mathrm{x,y,z}\}=\{\vartheta^{\mathrm{NR}}, \tilde{\vartheta}, \vartheta\}$, this derivation provides an equivalent skill definition: a positive skill means the FM anomaly quantity ϑ explains the analogous NR field ϑ^{NR} to a greater extent, and vice versa, after data assimilation.

APPENDIX B

B1. Atmospheric pressure uncertainty

In Section 34, atmospheric pressure uncertainty was derived from the standard deviation of JRA-55 data, but other formulations may be valid. Take for example Fig.B1a, which, like Fig. 9, shows a potential uncertainty field $\sigma_{p_{\mathrm{atm}}}$ whose inverse square weights atmospheric pressure adjustments in an adjoint-based least squares data assimilation. Like the uncertainty fields used to weight control adjustments in ASTEr1, $\sigma_{p_{\mathrm{atm}}}$ are constructed following Chaudhuri et al. (2014): the field is derived from the spread of p_{atm} values for the month of January 2012 across multiple atmospheric reanalysis products, namely JRA-55, the fifth generation ECMWF atmospheric reanalysis (ERA5, Dee et al. 2011), and the Japanese Reanalysis for Three Quarters of a Century (JRA-3Q, Kosaka et al. 2024). Fig. B1b shows the 90th percentile values of the magnitude of the atmospheric pressure adjustment seen after 20 iterations (i.e. the absolute value of Fig. 10d) normalized by $\sigma_{p_{\mathrm{atm}}}$. The atmospheric pressure adjustment is within .1 standard deviations of the p_{atm} uncertainty, thus confirming reasonable adjustment magnitudes.

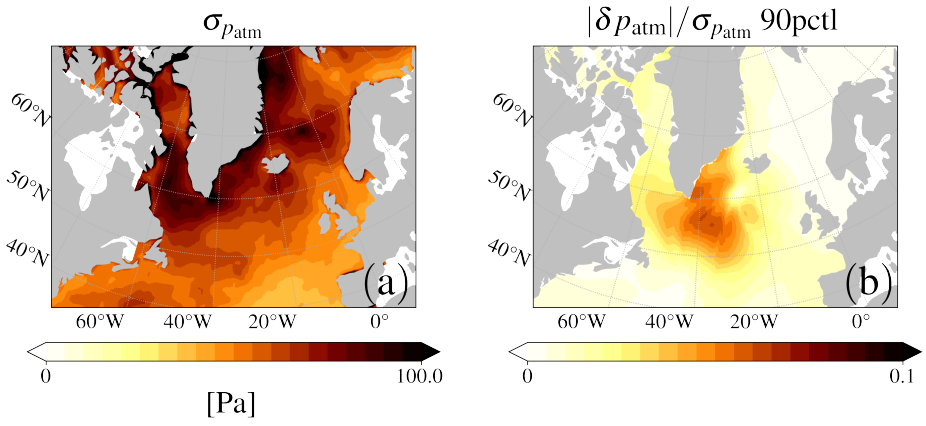

FIG. B1. (a) Atmospheric pressure uncertainty whose inverse square weights atmospheric pressure adjustments δp_{atm}. (b) The 90th percentile of p_{atm} adjustments scaled by $\sigma_{p_{\mathrm{atm}}}$ are small, indicating that the adjustments are, at least in magnitude, physical.

Using this p_{atm} uncertainty field, the Subpolar Gyre January OSSE is repeated, and the same mechanism in Fig. 10 is present once again (not shown): the negative-positive atmospheric pressure adjustment counterbalances and reduces the positive-negative spatial misfit dipole.

APPENDIX C

C1. GRACE-equivalent synthetic data processing

Here we describe additional steps performed to generating synthetic GRACE data, p_b^{GRACE}, from the NR used in the GRACE_annual OSSE. Monthly means were first computed from daily p_b^{syn} data on the $1/3°$ grid before aggregating these data into blocks of side length roughly 300 km (nominally 3°) reflecting the footprint of GRACE's mass concentration blocks ("mascons"). For this final step, a mascons map was obtained from GRACE data from each month of 2012 and mapped onto the ECCO $1/3°$ global grid (Zhang et al. 2018). Clusters of grid cells sharing a common value were assigned an index, which was then used to bin-average the monthly mean p_b data. For consistency, we reconstruct the p_b representation error covariance $\mathbf{\Gamma}_{\mathrm{obs}}$ by modifying the procedure in Section 2d to compute the standard deviation over monthly-averaged – rather than daily-averaged – NR records.

APPENDIX D

D1. Sensor spacing

Cable sensor placement will be guided by industry standards, and is therefore not the focus of this study. However, a preliminary set of experiments confirm that denser arrays achieve denser p_b skill for month long OSSEs. Fig. D1 shows p_b skill from the January 2012 OSSE after 10 iterations with all controls active repeated for SPNA cables with 70, 140, and 210 km sensor spacing. The misfit costfunctions used smoothing (**S**, Section 2d) length 100 km, and were repeated with smoothing length 300 km (not shown). The decreased smoothing scale permits more localized control adjustments and in turn p_b skill. The sparser cables were generated using a nearest neighbor resampling routine applied to the 70 km cable. Fig. D1 shows p_b skill *differences* between (a) 70–140, (b) 70–210, and (c) 140–210 km experiments. Green regions in all subplots indicate that in general, denser SMART cables improve p_b representation. In North Sea, however, control and resultant p_b adjustments are sensitive to how neighboring sensor misfits blend during smoothing, meaning more p_b observations in this regions can destructively interfere with one another. Future sensor spacing experiments should more closely examine these regions and their sensitivity to the smoothing length scale. Moreover, topographic gradients should inform cable design in favor of the naive downsampling performed here.

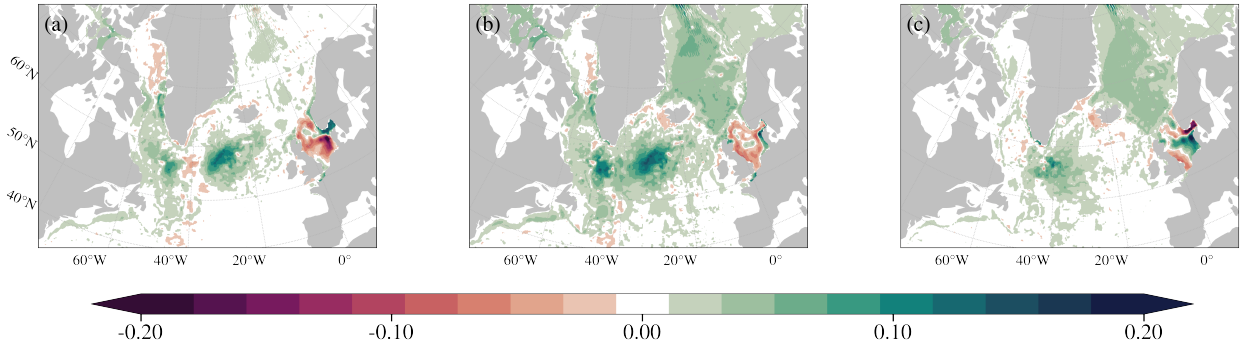

FIG. D1. January 2012 OSSEs are repeated for SPNA cables with sensor spacings of 70, 140, and 210 km and are shown as p_b skill differences between experiments: (a) 70–140, (b) 70–210, and (c) 140–210 km.

Acknowledgments.

This work was supported by the Gordon and Betty Moore Foundation through Grant GBMF10787. The adjoint model was generated using the AD tool Transformation of Algo-

rithms in Fortran (TAF) by Fastopt. AN and HP received additional support from NSF AccelNet program, Award #2114717 and Jet Propulsion Laboratory, California Institute of Technology (JPL/ Caltech) Subcontract ("ECCO- Connections").

Data availability statement.

The nature run data is accessible from ECCO's public data portal (`https://data.nas.nasa.gov/ecco/llc_4320/`) and via the Poseidon Project (Haine 2025). The forecast model is a configuration of ASTEr1, available at the Arctic Data Center (`https://arcticdata.io/catalog/portals/ASTE/ASTE`). The JRA-55 forcing dataset can be downloaded at (`https://climatedataguide.ucar.edu/climate-data/jra-55`). Modifications to the forecast model configuration, nature run extraction scripts, and data processing and analysis routines are available on GitHub (`https://github.com/mgoldberg10/smartosse`).

References

Adcroft, A., C. Hill, J.-M. Campin, J. Marshall, and P. Heimbach, 2004: Overview of the formulation and numerics of the MIT GCM. *Proceedings of the ECMWF Seminar on Recent Developments in Numerical Methods for Atmospheric and Ocean Modelling*, ECMWF, Reading, United Kingdom, 139–150.

Arbic, B. K., 2022: Incorporating tides and internal gravity waves within global ocean general circulation models: A review. *Prog. Oceanogr.*, **206**, 102 824, https://doi.org/10.1016/j.pocean.2022.102824.

Avsic, T., U. Send, and E. Skarsoulis, 2005: Six years of tomography observation in the central labrador sea. *International Conference Underwater Acoustic Measurements: Technologies and Results*, Heraklion, Greece, [Invited talk].

Bacon, S., A. C. Naveira Garabato, Y. Aksenov, N. J. Brown, and T. Tsubouchi, 2022: Arctic ocean boundary exchanges: A review. *Oceanography*, **35 (4)**, https://doi.org/10.5670/oceanog.2022.133.

Blazquez, A., B. Meyssignac, J. Lemoine, E. Berthier, A. Ribes, and A. Cazenave, 2018: Exploring the uncertainty in GRACE estimates of the mass redistributions at the Earth surface: implications for the global water and sea level budgets. *Geophys J Int*, **215 (1)**, 415–430, https://doi.org/https://doi.org/10.1093/gji/ggy293.

Campin, J.-M., A. Adcroft, C. Hill, and J. Marshall, 2004: Conservation of properties in a free-surface model. *Ocean Modelling*, **6**, 221–244, https://doi.org/10.1016/S1463-5003(03)00009-X.

Chaudhuri, A. H., R. M. Ponte, and A. T. Nguyen, 2014: A comparison of atmospheric reanalysis products for the arctic ocean and implications for uncertainties in air–sea fluxes. *J. Climate*, **27**, 5411–5421, https://doi.org/10.1175/JCLI-D-13-00424.1.

Chen, L., J. Yang, and L. Wu, 2023: Topography effects on the seasonal variability of ocean bottom pressure in the north pacific ocean. *J. Phys. Oceanogr.*, **53**, 929–941, https://doi.org/10.1175/JPO-D-22-0140.1.

Curry, B., C. M. Lee, B. Petrie, R. E. Moritz, and R. Kwok, 2014: Multiyear volume, liquid freshwater, and sea ice transports through davis strait, 2004–10. *J. Phys. Oceanogr.*, **44**, 1244–1266, https://doi.org/10.1175/JPO-D-13-0177.1.

Dee, D. P., S. M. Uppala, A. J. Simmons, P. Berrisford, P. Poli, and S. Kobayashi, 2011: The era-interim reanalysis: Configuration and performance of the data assimilation system. *Quart. J. Royal Meteor. Soc.*, **137**, 553–597, https://doi.org/10.1002/qj.828.

Douville, H., and Coauthors, 2021: Water cycle changes. *Climate Change 2021: The Physical Science Basis*, V. Masson-Delmotte, P. Zhai, A. Pirani, S. L. Connors, C. Péan, S. Berger, Y. Caud, Y. Chen, L. Goldfarb, M. I. Gomis, M. Huang, K. Leitzell, E. Lonnoy, J. B. R. Matthews, T. K. Maycock, T. Waterfield, O. Yelekçi, R. Yu, and B. Zhou, Eds., Cambridge University Press, Cambridge, United Kingdom and New York, NY, USA, 1055–1210, https://doi.org/10.1017/9781009157896.010.

Forget, G., J.-M. Campin, P. Heimbach, C. N. Hill, R. M. Ponte, and C. Wunsch, 2015: ECCO version 4: an integrated framework for non-linear inverse modeling and global ocean state estimation. *Geosci. Model Dev.*, **8**, 3071–3104, https://doi.org/10.5194/gmd-8-3071-2015.

Foukal, N., I. Le Bras, Y. Fu, T. Petit, B. T. C., S. Elipot, and B. Moat, 2026: Strengthening connections in observing the north atlantic meridional overturning circulation: Oucomes from a joint rapid-osnap workshop. *Oceanography*.

Fukumori, I., O. Wang, I. Fenty, G. Forget, P. Heimbach, and R. Ponte, 2017: Ecco central estimate (version 4 release 3). MITgcm-based ocean state estimate, https://ecco-group.org/products-ECCO-V4r3.htm.

Fukumori, I., O. Wang, W. Llovel, I. Fenty, and G. Forget, 2015: A near-uniform fluctuation of ocean bottom pressure and sea level across the deep ocean basins of the arctic ocean and the nordic seas. *Prog. Oceanogr.*, **134**, 152–172, https://doi.org/10.1016/j.pocean.2015.01.013.

Gallmeier, K., J. X. Prochaska, P. Cornillon, D. Menemenlis, and M. Kelm, 2013: An evaluation of the LLC4320 global-ocean simulation based on the submesoscale structure of modeled sea surface temperature fields. *Geosci. Model Dev.*, **16**, 7143–7170, https://doi.org/10.5194/gmd-16-7143-2023.

Giering, R., and T. Kaminski, 1998: Recipes for adjoint code construction. *ACM Trans. on Math. Software*, **24**, 437–474, https://doi.org/10.1145/293686.293695.

Haine, T., 2025: Democratize the data: A new way to analyze and design ocean models. *Oceanography*, **38 (3)**, https://doi.org/10.5670/oceanog.2025.e303.

Haine, T. W., and Coauthors, 2015: Arctic freshwater export: Status, mechanisms, and prospects. *Global Planet. Change*, **125**, 13–35, https://doi.org/10.1016/j.gloplacha.2014.11.013.

Haine, T. W. N., 2020: Arctic ocean freshening linked to anthropogenic climate change: All hands on deck. *Geophys. Res. Lett.*, **47 (23)**, e2020GL090 678, https://doi.org/10.1029/2020GL090678.

Handmann, P., J. Fischer, M. Visbeck, J. Karstensen, A. Biastoch, C. Böning, and L. Patara, 2018: The deep western boundary current in the labrador sea from observations and a high-resolution model. *J. Geophys. Res. Oceans*, **123**, 2829–2850, https://doi.org/10.1002/2017JC013702.

Hoffman, R., and R. Atlas, 2015: Future observing system simulation experiments. *Bull. Amer. Meteor. Soc.*, **97**, 1601—-1616, https://doi.org/10.1175/BAMS-D-15-00200.1.

Howe, B. M., and Coauthors, 2019: Smart cables for observing the global ocean: Science and implementation. *Front. Mar. Sci.*, **6**, https://doi.org/10.3389/fmars.2019.00424.

Hughes, C. W., M. E. Tamisiea, R. J. Bingham, and J. Williams, 2012: Weighing the ocean: Using a single mooring to measure changes in the mass of the ocean. *Geophys. Res. Lett.*, **39**, L17 602, https://doi.org/10.1029/2012GL052935.

Jahn, A., L. B. Tremblay, R. Newton, M. M. Holland, L. A. Mysak, and I. A. Dmitrenko, 2010: A tracer study of the arctic ocean's liquid freshwater export variability. *J. Geophys. Res. Oceans*, **115 (C7)**, https://doi.org/10.1029/2009JC005873.

Jones, D. C., G. Forget, B. Sinha, S. A. Josey, E. J. D. Boland, A. J. S. Meijers, and E. Shuckburgh, 2018: Local and remote influences on the heat content of the labrador sea: An adjoint sensitivity study. *J. Geophys. Res. Oceans*, **123**, 2646–2667, https://doi.org/10.1002/2018JC013774.

JTF Engineering Team, 2016: General requirements for sensor enabled reliable telecommunications (SMART) cable systems. White Paper Issue 1.0, Joint Task Force on SMART Cable Systems.

King, M., I. Howat, S. Candela, and Coauthors, 2020: Dynamic ice loss from the Greenland Ice Sheet driven by sustained glacier retreat. *Commun. Earth Environ.*, **1**, https://doi.org/10.1038/s43247-020-0001-2.

Kobayashi, S., and Coauthors, 2015: The JRA-55 reanalysis: General specifications and basic characteristics. *J. Meteor. Soc. Japan*, **93 (1)**, 5–48, https://doi.org/10.2151/jmsj.2015-001.

Kosaka, Y., and Coauthors, 2024: The JRA-3Q reanalysis. *J. Meteor. Soc. Japan*, **102**, 49–109, https://doi.org/10.2151/jmsj.2024-004.

Kostov, Y., and Coauthors, 2021: Distinct sources of interannual subtropical and subpolar Atlantic overturning variability. *Nat. Geosci.*, **14**, 491–495, https://doi.org/https://doi.org/10.1038/s41561-021-00759-4.

Köhl, A., F. Siegismund, and D. Stammer, 2012: Impact of assimilating bottom pressure anomalies from grace on ocean circulation estimates. *J. Geophys. Res. Oceans*, **117**, C04 032, https://doi.org/https://doi.org/10.1029/2011JC007623.

Lammers, R. B., A. I. Shiklomanov, C. J. Vörösmarty, B. M. Fekete, and B. J. Peterson, 2001: Assessment of contemporary arctic river runoff based on observational discharge records. *Journal of Geophysical Research: Atmospheres*, **106 (D4)**, 3321–3334, https://doi.org/https://doi.org/10.1029/2000JD900444.

Landerer, F. W., F. M. Flechtner, H. Save, F. H. Webb, T. Bandikova, W. I. Bertiger, and et al., 2020: Extending the global mass change data record: GRACE follow-on instrument and science data performance. **47**, https://doi.org/10.1029/2020GL088306.

Landerer, F. W., J. H. Jungclaus, and J. Marotzke, 2007: Ocean bottom pressure changes lead to a decreasing length-of-day in a warming climate. *Geophysical Research Letters*, **34 (6)**, https://doi.org/https://doi.org/10.1029/2006GL029106.

Li, F., Y. Fu, M. S. Lozier, I. A. L. Bras, M. F. de Jong, Y. Wang, and A. Sanchez-Franks, 2024: Deep circulation variability through the eastern subpolar north atlantic. *J. Climate*, **37 (23)**, https://doi.org/10.1175/JCLI-D-23-0487.1.

Loose, N., and P. Heimbach, 2021: Leveraging uncertainty quantification to design ocean climate observing systems. *J. Adv. Model. Earth Sy.*, **13**, e2020MS002 386, https://doi.org/https://doi.org/10.1029/2020MS002386.

Loose, N., P. Heimbach, H. R. Pillar, and K. H. Nisancioglu, 2020: Quantifying dynamical proxy potential through shared adjustment physics in the north atlantic. *J. Geophys. Res. Oceans*, **125 (9)**, e2020JC016 112, https://doi.org/10.1029/2020JC016112.

Lozier, M. S., and Coauthors, 2017: Overturning in the subpolar north atlantic program: A new international ocean observing system. *Bull. Amer. Meteor. Soc.*, **98**, 737–752, https://doi.org/10.1175/BAMS-D-16-0057.1.

Marshall, J., A. Adcroft, C. Hill, L. Perelman, and C. Heisey, 1997: A finite-volume, incompressible Navier Stokes model for studies of the ocean on parallel computers. *J. Geophys. Res.*, **102**, 5753–5766, https://doi.org/10.1029/96JC02775.

Mercier, H., D. Desbruyères, P. Lherminier, A. Velo, L. Carracedo, M. Fontela, and F. F. Pérez, 2024: New insights into the eastern subpolar north atlantic meridional overturning circulation from OVIDE. *EGUsphere*, 1–27, https://doi.org/10.5194/egusphere-2024-388.

Münchow, A., and H. Melling, 2008: Ocean current observations from nares strait to the west of greenland: Interannual to tidal variability and forcing. *J. Mar. Res.*, **66**, 801–833, https://doi.org/10.1357/002224008788064612.

Na, H., D. R. Watts, J.-H. Park, C. Jeon, H. J. Lee, M. Nonaka, and A. D. Greene, 2016: Bottom pressure variability in the Kuroshio Extension driven by the atmosphere and ocean instabilities. **121**, 6507–6519, https://doi.org/10.1002/2016JC012097.

Nguyen, A. T., H. Pillar, V. Ocaña, A. Bigdeli, T. A. Smith, and P. Heimbach, 2021: The Arctic Subpolar Gyre sTate Estimate: Description and assessment of a data-constrained, dynamically consistent ocean-sea ice estimate for 2002–2017. *J. Adv. Model. Earth Sy.*, **13**, e2020MS002 398, https://doi.org/10.1029/2020MS002398.

Pacini, A., and R. S. Pickart, 2022: Meanders of the west greenland current near cape farewell. *Deep-Sea Res. I: Oceanogr. Res. Pap.*, **179**, https://doi.org/10.1016/j.dsr.2021.103664.

Ponte, R. M., 1992: The sea level response of a stratified ocean to barometric pressure forcing. *J. Phys. Oceanogr.*, https://doi.org/10.1175/1520-0485(1992)022⟨0109:TSLROA⟩2.0.CO;2.

Ponte, R. M., 1994: Understanding the relation between wind- and pressure-driven sea level variability. *J. Geophys. Res. Oceans*, **99**, https://doi.org/https://doi.org/10.1029/94JC00217.

Ponte, R. M., and J. Dorandeu, 2003: Uncertainties in ecmwf surface pressure fields over the ocean in relation to sea level analysis and modeling. *J. Atmos. Oceanic Technol.*, **20 (2)**, https://doi.org/10.1175/1520-0426(2003)020⟨0301:UIESPF⟩2.0.CO;2.

Ponte, R. M., E. N. S. Silva, O. Wang, I. Fukumori, and M. Zhao, 2026: Improving ocean bottom pressure fields using space gravity data in state estimation. *EGUsphere*, **2026-947**, https://doi.org/10.5194/egusphere-2026-947.

Quinn, K. J., and R. M. Ponte, 2011: Estimating high frequency ocean bottom pressure variability. *Geophysical Research Letters*, **38 (8)**, https://doi.org/https://doi.org/10.1029/2010GL046537.

Rocha, C. B., S. T. Gille, T. K. Chereskin, and D. Menemenlis, 2016: Seasonality of submesoscale dynamics in the kuroshio extension. *Geophys. Res. Lett.*, **43**, 11,304–11,311, https://doi.org/10.1002/2016GL071349.

Saynisch, J., I. Bergmann, and M. Thomas, 2015: Assimilation of grace-derived oceanic mass distributions with a global ocean circulation model. *J. Geodesy*, **89 (2)**, 121–139, https://doi.org/10.1007/s00190-014-0766-0.

Serreze, M. C., and W. N. Meier, 2019: The Arctic's sea ice cover: trends, variability, predictability, and comparisons to the Antarctic. *Annals of the New York Academy of Sciences*, **1436 (1)**, 36–53, https://doi.org/https://doi.org/10.1111/nyas.13856.

Shiklomanov, A., S. Déry, M. Tretiakov, D. Yang, D. Magritsky, A. Georgiadi, and W. Tang, 2021: *River Freshwater Flux to the Arctic Ocean*, 703–738. https://doi.org/10.1007/978-3-030-50930-9_24.

Stammer, D., K. Ueyoshi, A. Köhl, W. G. Large, S. A. Josey, and C. Wunsch, 2004: Estimating air-sea fluxes of heat, freshwater, and momentum through global ocean data assimilation. *J. Geophys. Res. Oceans*, **109**, C05 023, https://doi.org/10.1029/2003JC002082.

Stepanov, V. N., and C. W. Hughes, 2006: Propagation of signals in basin-scale ocean bottom pressure from a barotropic model. *J. Geophys. Res. Oceans*, **111 (C12)**, 002, https://doi.org/ https://doi.org/10.1029/2005JC003450.

Tapley, B. D., S. Bettadpur, M. Watkins, and C. Reigber, 2004: The gravity recovery and climate experiment: Mission overview and early results. *Geophys. Res. Lett.*, **31**, https://doi.org/10.1029/ 2004GL019920.

Tapley, B. D., and Coauthors, 2019: Contributions of GRACE to understanding climate change. *Nat. Clim. Change*, **5**, 358–369, https://doi.org/10.1038/s41558-019-0456-2.

Wang, J., L.-L. Fu, B. Qiu, D. Menemenlis, J. T. Farrar, Y. Chao, A. F. Thompson, and M. M. Flexas, 2018: An observing system simulation experiment for the calibration and validation of the surface water ocean topography sea surface height measurement using in situ platforms. *J. Atmos. Oceanic Technol.*, **35 (2)**, 281–297, https://doi.org/10.1175/JTECH-D-17-0076.1.

Weiss-Gibbons, T., A. Tefs, X. Hu, T. Stadnyk, and P. G. Myers, 2024: Sensitivity of simulated arctic ocean salinity and strait transport to interannually variable hydrologic model based runoff. *J. Geophys. Res. Oceans*, e2023JC020536, https://doi.org/10.1029/2023JC020536.

Weijer, W., T. Haine, A. Siddiqui, W. Cheng, M. Veneziani, and P. Kurtakoti, 2022: Interactions between the arctic mediterranean and the atlantic meridional overturning circulation: A review. *Oceanography*, **35**, 118–127, https://doi.org/https://doi.org/10.5670/oceanog.2022.130.

Wunsch, C., and P. Heimbach, 2007: Practical global oceanic state estimation. *Phys. D: Nonlinear Phenom.*, **230**, 197–208, https://doi.org/10.1016/j.physd.2006.09.040.

Zeng, X., and Coauthors, 2020: Use of observing system simulation experiments in the United States. *Bull. Amer. Meteor. Soc.*, **101 (8)**, E1427–E1438, https://doi.org/10.1175/ BAMS-D-19-0155.1.

Zhang, H., D. Menemenlis, and I. Fenty, 2018: ECCO LLC270 Ocean-Ice State Estimate. URL http://hdl.handle.net/1721.1/119821, ECCO Consortium. accessed 1 Aug 2025.

Zhang, J., and L. Du, 2025: Freshwater transport variation through Fram and Davis Strait influenced by atmospheric circulation. *Front. Mar. Sci.,*, **12**, https://doi.org/10.3389/fmars.2025.1608187.

Zhang, J., W. Weijer, M. Steele, and Coauthors, 2021: Labrador sea freshening linked to beaufort gyre freshwater release. *Nat. Commun.*, **12**, 1229, https://doi.org/10.1038/s41467-021-21470-3.